small methods
www.small-methods.com

Recent Progress on Wavelength-Selective Perovskite Photodetectors for Image Sensing

*Wenqiang Wu, Hui Lu, Xun Han, Chunfeng Wang, Zhangsheng Xu, Su-Ting Han, and Caofeng Pan**

Spectral sensing plays a crucial part in imaging technologies, optical communication, and other fields. However, complicated optical elements, such as prisms, interferometric filters, and diffraction grating, are required for commercial multispectral detectors, which hampers their advance toward miniaturization and integration. In recent years, metal halide perovskites have been emerging for optical-component-free wavelength-selective photodetectors (PDs) because of their continuously tunable bandgap, fascinating optoelectronic properties, and simple preparation processes. In this review, recent advances in wavelength-selective perovskite PDs, including narrowband PDs, dual-band PDs, multispectral-recognizable PDs, and X-ray PDs, are highlighted, with an emphasis on device structure designs, working mechanisms, and optoelectronic performances. Meanwhile, the applications of wavelength-selective PDs in image sensing for single-/dual-color imaging, full-color imaging, and X-ray imaging are introduced. Finally, the remaining challenges and perspectives in this emerging field are presented.

1. Introduction

Wavelength-selective photodetectors (PDs) are responsive to lights of particular wavelengths or in a specific band window, which has extensive applications in image sensing, optical communication, and environment monitoring.[1–5] Among them, visible PDs and X-ray PDs have attracted more attention due to today's ever-increasing demand for imaging technologies in the fields of machine vision and X-ray tomography.[6–9] Generally, the wavelength recognition in commercial visible image sensors is enabled by the integration of silicon (Si)-based PDs and Bayer filters, in which the Bayer filters with a 2 × 2 red-green-blue-green pattern (RGBG) for each pixel are placed on the top of the PD arrays, complicating the device fabrication and challenging the high-density integration.[10,11] Additionally, the rigidness of Si materials limits the development of future flexible image sensors.[12] Regarding X-ray imaging, a long imaging time is usually required for the amorphous selenium (α-Se) direct-conversion detector due to the low X-ray stopping ability and insufficient charge transport.[13] And scintillator imagers based on traditional scintillators usually suffer from poor image quality due to low conversion efficiency and scattering-induced optical crosstalk.[14] Moreover, some of the traditional scintillators, such as agglomerated powders and bulk crystals, need to be sintered at high temperatures, and their luminescence is difficult to adjust in the visible region due to afterglow effects.[15,16]

In recent years, the metal halide perovskites have emerged as promising materials for wavelength-selective PDs due to their excellent optoelectronic properties, including strong light absorption, low defect states density, decent carrier mobility, continuously tunable bandgap, and so on.[5,17–20] Lin et al. first reported the filterless narrowband PDs by employing solution-processable mixed lead halide perovskites.[21] The narrowband PDs with the spectral response from blue to red and full width at half maximum (FWHM) of < 100 nm were achieved by adjusting the halide compositions. Furthermore, metal halide perovskites could be applied to direct X-ray detection or as a scintillator.[22] As early as 2015, Yakunin et al. demonstrated the direct-conversion X-ray detectors based on solution-processed $CH_3NH_3PbI_3$ perovskite films with an X-ray sensitivity of 25 μC mGy_{air}^{-1} cm^{-3}.[23] Subsequently, a series of perovskite-based wavelength-selective PDs with novel structures and mechanisms have been explored and considerable progress has been achieved.[24–27] Therefore, a review of wavelength-selective perovskite PDs is imperative to promote the development of this research field.

This review starts with the introduction of the performance metrics for wavelength-selective PDs. And then, four-type of metal halide perovskite wavelength-selective PDs are

W. Wu, X. Han, S.-T. Han
Institute of Microscale Optoelectronics
Shenzhen University
Shenzhen 518060, P. R. China

W. Wu, H. Lu, Z. Xu, C. Pan
CAS Center for Excellence in Nanoscience
Beijing Key Laboratory of Micro-Nano Energy and Sensor
Beijing Institute of Nanoenergy and Nanosystems
Chinese Academy of Sciences
Beijing 100083, P. R. China
E-mail: cfpan@binn.cas.cn

C. Wang
College of Materials Science and Engineering
Guangdong Research Center for Interfacial Engineering of Functional Materials
Shenzhen University
Shenzhen 518060, P. R. China

The ORCID identification number(s) for the author(s) of this article can be found under https://doi.org/10.1002/smtd.202201499

DOI: 10.1002/smtd.202201499

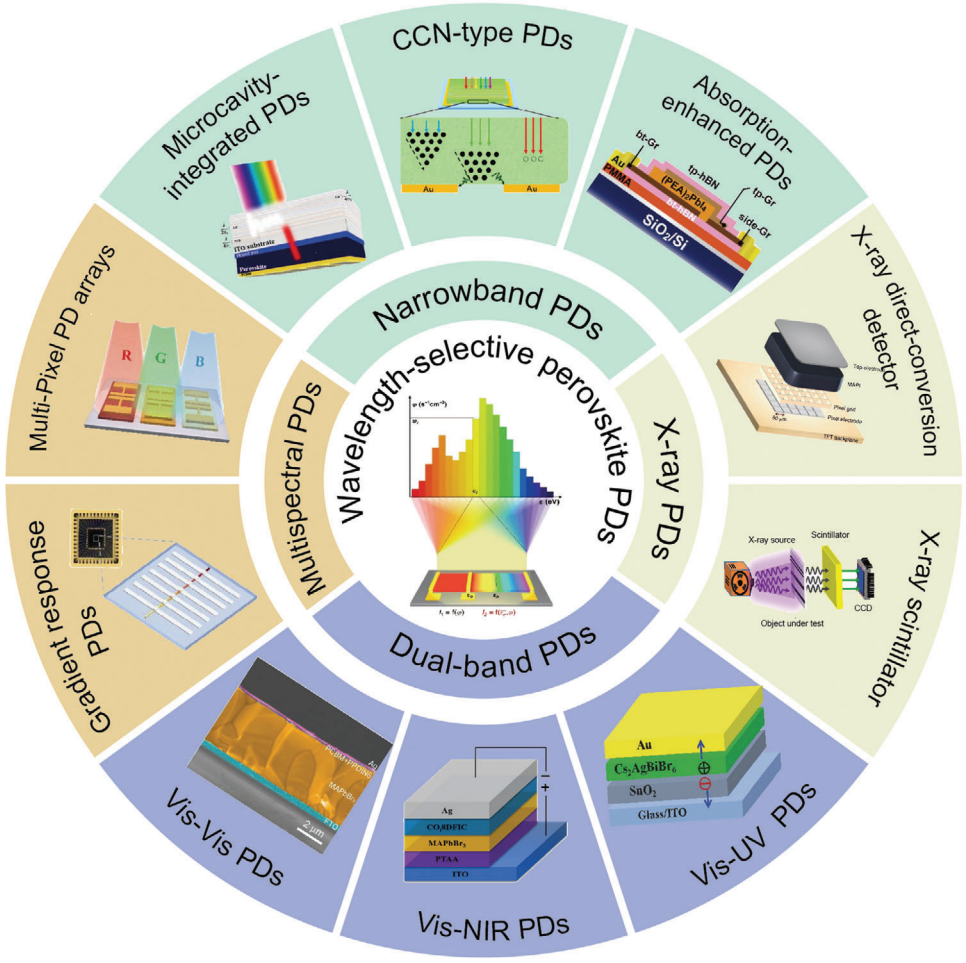

Figure 1. Schematically demonstrating types of wavelength-selective perovskite PDs, including narrowband PDs, dual-band PDs, multispectral-recognizable PDs, and X-ray PDs. "Wavelength-selective perovskite PDs": Reproduced with permission.[93] Copyright 2020, Springer Nature. "Microcavity-integrated PDs": Reproduced with permission.[74] Copyright 2019, Wiley-VCH. "CCN-type PDs": Reproduced with permission.[56] Copyright 2018, American Chemical Society. "Absorption-enhanced PDs": Reproduced with permission.[54] Copyright 2020, Wiley-VCH. "X-ray direct-conversion detector": Reproduced with permission.[115] Copyright 2021, Springer Nature. "X-ray scintillator": Reproduced with permission.[118] Copyright 2022, Wiley-VCH. "Vis–UV PDs": Reproduced with permission.[79] Copyright 2020, Wiley-VCH. "Vis–NIR PDs": Reproduced with permission.[87] Copyright 2020, Wiley-VCH. "Vis–Vis PDs": Reproduced with permission.[80] Copyright 2021, Wiley-VCH. "Gradient response PDs": Reproduced with permission.[40] Copyright 2021, Wiley-VCH. "Multipixel PD arrays": Reproduced with permission.[96] Copyright 2021, Wiley-VCH.

summarized, including narrowband PDs, dual-band PDs, multispectral-recognizable PDs, and X-ray PDs (**Figure 1**). The structures, working mechanisms, and performances of these devices are comprehensively discussed, along with their applications in image sensing of single-/dual-color imaging, full-color imaging, and X-ray imaging. Finally, perspectives on the key challenges and future directions of the wavelength-selective PDs are presented.

2. Performance Metrics of Wavelength-Selective PDs

PD is a kind of device that converts optical signals into electrical signals. To quantitatively evaluate the performance of PDs, the fundamental performance metrics are defined. In this section, the key performance parameters of the normal wavelength-selective PDs (narrowband PDs, dual-band PDs, and multispectral-recognizable PDs) and X-ray PDs are summarized, respectively.

2.1. Key Performance Parameters of the Normal Wavelength-Selective PDs

Responsivity (R): R is defined as the ratio of the photogenerated current of the PDs to the incident light power intensity, which represents the photoelectric conversion capability of PDs. The formula is as follows

$$R = \frac{I_{ph}}{P_{in}S} = \frac{I_{light} - I_{dark}}{P_{in}S} \quad (1)$$

I_{ph}, I_{light}, and I_{dark} represent the photogenerated current, the current of PD under illumination, and the current of the PD in dark

conditions, respectively. P_{in} is the power density of incident light. S is the effective area of the PD exposed to light.

External Quantum Efficiency (EQE): EQE is described as the ratio of the number of photogenerated carriers to the number of incident photons on PD, which can be expressed as follows

$$EQE = \frac{N_C}{N_I} = \frac{hc}{e\lambda} R \tag{2}$$

N_C and N_I represent the number of photogenerated carriers and incident photons, respectively. h, c, e, and λ are the Planck constant, the light speed, the electron charges, and the wavelength of the incident light, respectively.

Noise Equivalent Power (NEP): The noise determines the PD's detection limit for light signal. NEP is defined as incident light power at the signal-to-noise ratio of 1 when the bandwidth of noise measurement is 1, which can be calculated by the following equation

$$NEP = \frac{i_n}{R} \tag{3}$$

i_n represents the noise current.

Specific Detectivity (D^*): D^* is a key performance parameter used to assess the ability of a PD to detect weak optical signals, which is inversely related to NEP. The formula is as follows

$$D^* = \frac{(S\Delta f)^{1/2}}{\mathrm{NEP}} = \frac{R(S\Delta f)^{1/2}}{i_n} \tag{4}$$

Δf represents the bandwidth. The noise of PD comes from shot noise, thermal noise, generation-recombination noise, and so on.[28] If the whole device noise is mainly contributed by shot noise from the dark current. The formula can be simplified as follows

$$D^* = \frac{R}{(2eI_{dark}/S)^{1/2}} \tag{5}$$

Linear Dynamic Range (LDR): LDR represents the range in which the photogenerated current exhibits a linear relationship with the incident light intensity. It can be calculated by the following equation

$$LDR = 20\log\frac{P_{max}}{P_{min}} \tag{6}$$

P_{max} and P_{min} are the maximum and minimum incident light intensity that PD can detect in the linear range.

Response Time (τ): τ shows how fast the PD responds to incident light, including rise time (τ_{rise}) and decay time (τ_{decay}), which are defined as the time of current rising from 10% to 90% and decaying from 90% to 10% of the maximum photocurrent, respectively.

FWHM of R and EQE: It is commonly used to evaluate the selectivity of narrowband PD's spectral response. Narrowband PDs possess a significant responsivity in a narrow spectral range, which is referred to as the responsivity passband. The FWHM of the responsivity can be denoted as $FWHM_R$. The same concept also applies to characterize the narrowband response range by using the EQE, denoted as $FWHM_{EQE}$.

Spectral Rejection Ratios (SRR): The crosstalk of wavelength-sensitive PDs over different spectral regions can be evaluated by SRR, which is defined as the ratio of responsivity at the target wavelengths to the one at the untargeted reference wavelengths. It can be expressed by the equation[29]

$$SRR\ (\lambda_{target}, \lambda_{ref}) = \frac{R(\lambda_{target})}{R(\lambda_{ref})} \tag{7}$$

λ_{target} is the light wavelength within the target detection spectral range, λ_{ref} is the light wavelength outside the target detection spectral range.

2.2. Key Performance Parameters of the X-Ray Detector

2.2.1. Key Performance Parameters of the Direct-Conversion X-Ray Detector

Dark Current: Dark current, also called leakage current, is the intrinsic current of the direct-conversion X-ray detector without X-ray radiation. The influence of a large dark current on the direct-conversion X-ray detector mainly has the following aspects: 1) the large dark current could lead to large noise and drown out the electrical signals from the X-ray radiation, thus attenuating the sensitivity and detection limit; 2) the high dark current also can decrease the dynamic response range; 3) the large dark current fills the charge-storage capacity, easily causing the X-ray planar pixel detectors to reach the breakdown voltage of the thin film transistor (TFT).[30]

Sensitivity (S): X-ray sensitivity is a paramount performance parameter of direct-conversion X-ray detectors, representing the ability of an X-ray detector to convert X-ray photons into collected charges. The formula is defined as follows

$$S = \frac{I_p - I_d}{DA} \tag{8}$$

I_p and I_d are the photocurrent and the dark current of direct-conversion X-ray detectors under X-ray irradiation and in dark conditions, respectively. D is the X-ray dose rate. A is the effective detection area.

Detection Limit: The detection limit refers to the detectable minimum X-ray dose of direct-conversion X-ray detectors, which is defined as the equivalent dose rate that produces a response signal greater than three times the noise level.[31]

Furthermore, several figure-of-merit, including the absorption coefficient, chemical stability, signal-noise-ratio, and response speed, is also important for direct-conversion X-ray detectors.[32,33]

2.2.2. Key Performance Parameters of the Indirect-Conversion X-Ray Detector (Scintillator)

Light Yield: Light yield is an important parameter for the scintillator, which determines the X-ray sensitivity and detection limit

of the indirect-conversion X-ray detector. It is defined as the number of photons emitted per unit of energy absorbed by a scintillator when exposed to ionizing radiation. The number of photons emitted by the scintillator can be calculated by the following formula

$$N_{ph} = \frac{E}{\beta E_{gap}} \times SQ \quad (9)$$

N_{ph} is the number of photons emitted by the scintillator. E and E_{gap} represent the energy of incident X-ray photons and the bandgap of the scintillator, respectively. β represents the required average energy for generating one thermalized electron–hole pair. S and Q are the quantum efficiencies of the transport/luminescence stages, respectively.

Emission Wavelength: The emission wavelength of the scintillator is a parameter worthy of attention and optimization, which should match the spectral response peak of the corresponding detectors. The perfect emission wavelengths of the scintillator should be in the range of 500–600 nm for matching the α-Si based p-i-n photodiodes.[34,35]

Afterglow: Afterglow refers to the intensity of the radiation luminescence over a certain period after X-ray irradiation. The requirement for the duration time of afterglow is different in various applications, for example, the highest requirement for computed tomography is 0.1% @ 3 ms.[36] Because the signals are superimposed on the previous strong exposure, a prolonged afterglow could result in imaging artifacts.[37]

Additionally, the X-ray stopping power, linearity of scintillation response, radioresistance, and spatial/energy resolution are important figure-of-merit of the scintillator.[14]

3. Device Structures, Working Mechanisms, and Performances of Wavelength-Selective Perovskite PDs

The perovskite-based wavelength-selective PDs can be roughly divided into four categories: narrowband PDs, dual-band PDs, multispectral-recognizable PDs, and a special kind of X-ray PDs.[38–41] In this section, the device structures, working mechanisms, and performances are summarized and analyzed, according to the classification.

3.1. Narrowband Perovskite PDs

Narrowband PDs, as the most common wavelength-selective PDs, possess a wavelength response window within 100 nm or even less than 10 nm.[42,43] Commercial narrowband PDs composed of broadband semiconductor materials (e.g., Si, Indium Gallium Arsenide (InGaAs)) and optical filters suffer from limited spectral recognition range and cumbersome integration, hindering their further development.[44,45] To overcome this issue, organic semiconductors were adopted to prepare filter-free narrowband PDs.[46] However, due to intrinsic material characteristics, such as the high exciton binding energy and small carrier mobility, organic narrowband PDs still have shortcomings,[47,48] as follows: i) the construction of organic narrowband PDs usually relies on a pair of blended compounds for exciton dissociation, such as bulk heterojunctions, complicating the progress of device fabrication;[49] ii) organic narrowband PDs have small EQE and slow response speed; iii) the stability of signal output when the device runs for a long time needs to be further optimized.[50,51] In recent years, lead halide perovskites have been widely proven with properties beyond that of conventional semiconductor materials, shedding light on high-performance narrowband PDs.[52–55] Currently, a great deal of perovskite-based narrowband PDs have been demonstrated, and their construction strategy is as follows: i) charge collection narrowing (CCN) mechanism; ii) broadband perovskite PDs combining with bandpass filters or optical microcavity; iii) enhancement of light absorption in a narrow range.[54,56–58]

3.1.1. CCN Mechanism

The CCN mechanism-based narrowband PDs dissipate photocarriers excited by lights outside the target spectra though regulating the recombination of carriers.[21,59] The device type of narrowband PDs working with this mechanism mainly includes photoconductance and photodiode. The photoconductance-type devices with a simple structure require strictly the thickness of perovskite material, which usually is several micrometers or even a few hundred micrometers.[60] Xue et al. reported the narrowband photoconductances based on polycrystalline perovskite films, and its working mechanism is schematically demonstrated in **Figure 2**a.[56] Under the illumination of short-wavelength lights, the carriers were only generated on the top surface of perovskite films due to the short penetration depth of photons. These photogenerated carriers would be quenched by recombination during their diffusion to the bottom electrodes. However, the long-wavelength lights with strong penetration ability could excite the carriers in perovskite materials near the electrodes. These photogenerated carriers were collected to produce photocurrent, thus resulting in a narrowband spectral response. In this work, the authors synthesized $CsPbBr_3$ films with different thicknesses using the freeze-drying casting method (Figure 2b). With the increase of the perovskite film thickness, the photoresponse of the device decayed in the short wavelength range until it disappeared, as shown in Figure 2c. The device fabricated using 20 μm perovskite films presented a narrow response with FWHM of less than 12 nm. Meanwhile, a variety of narrowband PDs with response wavelengths in the visible region have also been demonstrated by adjusting the halide compositions (Figure 2d,e).

Compared with polycrystalline perovskite films, perovskite single crystals without grain boundaries have many advantages, such as high carrier mobility and low volume defect density, for fabricating narrowband PDs.[61,62] Fang et al. first applied perovskite single crystals ($MAPbBr_{3-x}Cl_x$ and $MAPbI_{3-x}Br_x$, MA = CH_3NH_3) to narrowband photoconductance.[63] The FWHM of spectral response ranging from blue to red was less than 20 nm. In this work, the working principle of surface charge recombination was proposed to explain the narrowband response. The perovskite single crystals prepared in solution introduced inevitable defects on the surface, which quenched the carriers excited by short wavelength lights. Therefore, the surface charge recombination effect suppressed the EQE in the short wavelength range, endowing the narrowband response characteristics of single-crystal perovskite photoconductance. Actually, the essence of the

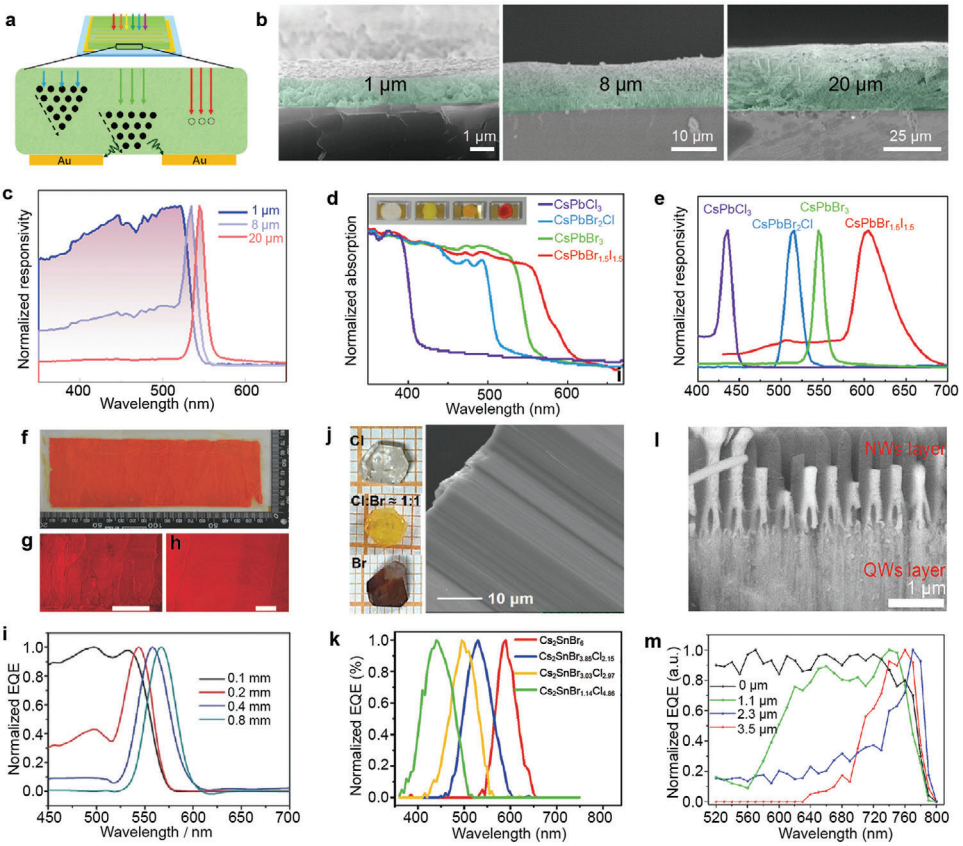

Figure 2. a) Schematic diagram of the CCN mechanism for the narrowband perovskite PD. b) SEM images of $CsPbBr_3$ films. c) Normalized responsivities of PDs fabricated with different thick perovskite films. d) Normalized absorption spectra of perovskite films with different elemental compositions. e) Normalized responsivities of $CsPbX_3$ PDs. a–e) Reproduced with permission.[56] Copyright 2018, American Chemical Society. f) The photograph of $CH_3NH_3PbBr_3$ crystal films. g) Bottom and h) top morphologies of $CH_3NH_3PbBr_3$ crystal films. Scale bar: 2 mm. i) Normalized EQE spectra of PDs fabricated with different thick perovskite films. f–i) Reproduced with permission.[60] Copyright 2017, Wiley-VCH. j) The photographs and SEM images of $Cs_2SnCl_{6-x}Br_x$ single crystals. k) Normalized EQE spectra of $Cs_2SnCl_{6-x}Br_x$ narrowband PDs. j,k) Reproduced with permission.[61] Copyright 2019, Wiley-VCH. l) SEM images of $MAPbI_3$ QWs/NWs. m) Normalized EQE spectra of PDs fabricated with different thick QWs layer. l,m) Reproduced with permission.[64] Copyright 2022, American Chemical Society.

surface charge recombination effect is still the CCN mechanism. According to this working principle, Rao et al. assembled narrowband photoconductance using large-scale $CH_3NH_3PbBr_3$ single crystals with a controllable thickness (Figure 2f–h).[60] Figure 2i shows the EQE spectra of the device related to the perovskite film thickness. With the increase of perovskite thickness, the spectral response of the PDs changed from broadband to narrowband. When the thickness of the perovskite film was 0.8 mm, the FWHM of spectral response was about 35 nm. In addition to organic–inorganic hybrid perovskite single crystals, all-inorganic perovskite single crystals have also been used as absorbing layers in narrowband PDs. Zhou et al. prepared Pb-free $Cs_2SnCl_{6-x}Br_x$ single crystals via the hydrothermal method (Figure 2j).[61] The narrowband PDs using these single crystals presented a high detectivity of 2.71×10^{10} Jones, and the narrow response peaks can alter from near violet to orange, as shown in Figure 2k. Besides, Zhang et al., for the first time, used perovskite single crystals nanowire/quantum wires for narrowband photoconductances (Figure 2l).[64] Based on the CCN mechanism, the photogenerated carriers in the short-wavelength range were lost due to radiative recombination in the quantum wires. As demonstrated in Figure 2m, the responsivity in the short-wavelength range was suppressed with the increase of the quantum wire length, and the narrowband response was finally realized at a quantum wire length of 3.5 μm.

2D perovskites with unique quantum-well structures possess self-trapped states due to the strong electron–phonon coupling, which booms the performances of narrowband PDs.[65,66] As shown in **Figure 3**a, Li et al. reported the narrowband photoconductances using 2D perovskite single crystals of $(BA)_2(MA)_{n-1}Pb_nX_{3n+1}$ ($BA = C_4H_9NH_3$; X = Br, I) and proposed the self-trapped state-assisted CCN mechanism.[67] To explore the mechanism of narrowband spectral response, three kinds of devices with different configurations were designed and the schematic diagram of the carrier generation and extraction process is displayed in Figure 3b. The EQE spectrum of config. 3 showed a broadband response with distinct three peaks of B, X_0, and X_t, which could be assigned to band-to-band transition peak, free-exciton peak, and self-trapped state-induced absorption peak, respectively (Figure 3c). The X_t peak observed in config. 3 matched well with the one of devices with config. 1 and config. 2, which proved that the self-trapped states of 2D perovskite

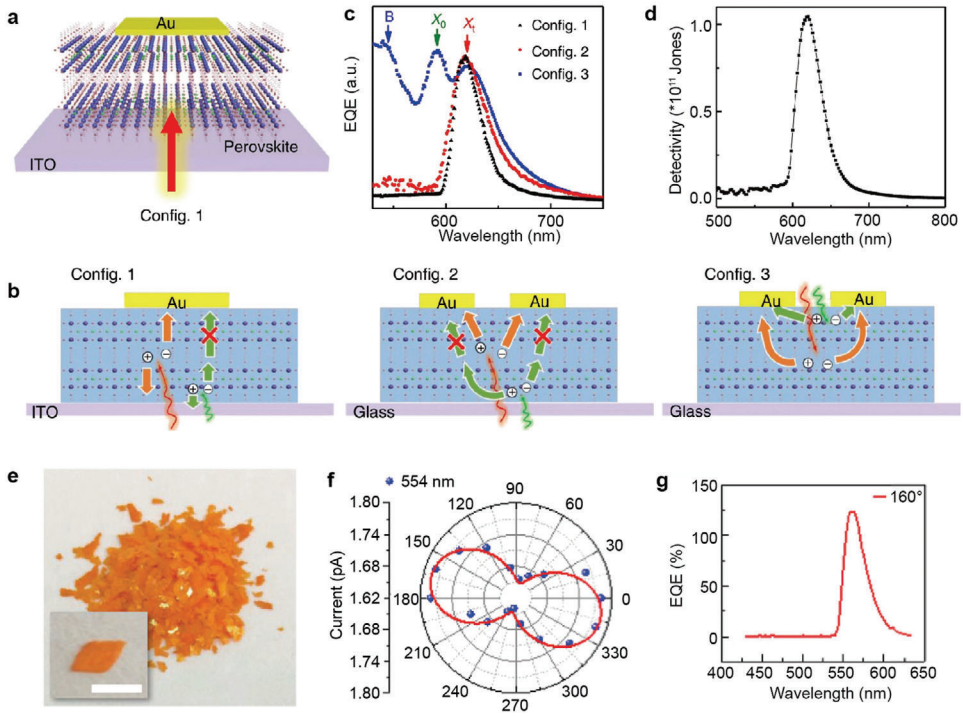

Figure 3. a) The structure of narrowband PDs based on 2D perovskite of $(BA)_2(MA)Pb_2I_7$. b). Schematic illustration of the carrier generation and separation of PDs with different configurations. c) EQE curves of devices with different structures. d) Specific detectivity of PD with config.1. a–d) Reproduced with permission.[67] Copyright 2019, Springer Nature. e) The photograph of (*iso*-$BA)_2PbI_4$ crystals. f) Variation of photocurrent with polarization angle. g) The specific detectivity of the device under the polarization angle of 160°. e–g) Reproduced with permission.[52] Copyright 2019, Wiley-VCH.

caused the narrowband response. The maximum specific detectivity of these narrowband PDs was as high as 1×10^{11} Jones, which is five times larger than that of the 3D single-crystal perovskite narrowband PDs, as presented in Figure 3d.[63] By adjusting the halide composition X and perovskite layer number n, the narrowband response peaks can be continuously tuned in the visible range, and the FWHM of all devices' spectral response was less than 60 nm. In addition, the polarization-sensitive narrowband PDs based on 2D $(BA)_2PbI_4$ perovskite single crystals have been reported as well (Figure 3e).[52] In this report, the device realized the dual functions of optical sensing for the polarization and spectra, ascribing to the large anisotropic crystal structure of the synthesized 2D perovskites and the CCN working mechanism. The polarization-dependent photocurrent identified the photoresponse anisotropy (Figure 3f). The response spectrum demonstrated a narrow response with a peak around 560 nm and an FWHM of 27 nm as presented in Figure 3g. And the maximum EQE was as high as 120% at a polarization angle of 160°.

Perovskite narrowband photodiodes possess a vertical structure similar to solar photovoltaic devices, where the perovskite material is sandwiched between an electron transport layer (ETL) and a hole transport layer (HTL).[68,69] Wang et al. first reported the self-powered narrowband photodiodes, as presented in **Figure 4**a.[70] Interestingly, the device exhibited a broadband response behavior at first, even with perovskite film thicknesses up to 25.1 µm, as displayed in Figure 4b. The photoresponse declined at the short-wavelength range after irradiation with 532 nm light for a few minutes (Figure 4c). The thicker the perovskite film, the more pronounced the phenomenon. After laser illumination, the device with a 25.1 µm perovskite film showed a narrow spectral response with an FWHM of around 29 nm. The space-charge-limited current (SCLC) measurements revealed that trap density in the perovskite films increased after illumination. The surface defect states determined the recombination of the charge carriers generated in the short wavelength range. As demonstrated in Figure 4d,e, the operating principle of the device still followed the CCN mechanism. In addition, Hou et al. proposed an unbalanced charge carrier transport strategy to tune carrier recombination for constructing narrowband photodiodes.[71] This strategy triggered the wavelength-dependent carrier collection, but not sacrificed charge transport properties, which is different from the reported way by enhancing the perovskite thickness to obtain narrowband PDs. In this strategy, the p-type mixed-halide perovskite films (p-$MAPbI_2Br$) were synthesized by a self-doping method. The photodiodes with inverted and normal structures were designed and both of which exhibited narrowband photoresponses with spectral response peaks at 625 and 350 nm, respectively (Figure 4f–i). The working principle of the invert-structured device is schematically shown in Figure 4j,k. The short-wavelengths photoexcited carriers were close to the HTL owing to the Beer–Lambert regime.[72] Although the holes were easily extracted, the electrons that reached the ETL can be ignored due to the low electron mobility in p-type $MAPbI_2Br$. In contrast, red lights deeply penetrated inside the perovskite and made charge carriers generated close to the ETL. In such a case, the short transport path and high hole mobility ensured that both

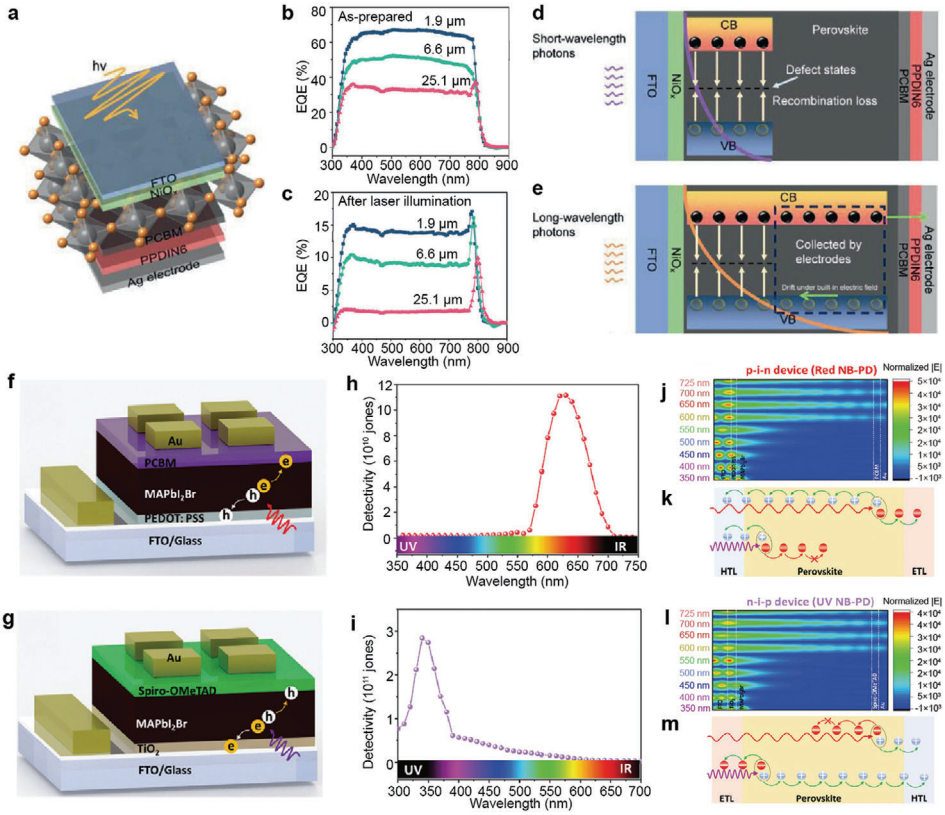

Figure 4. a) Device architecture of the self-drive narrowband photodiode devices. b) EQE spectra of the as-prepared device with different thick perovskite layers. c) EQE spectra of the device after laser illumination. d,e) Schematic diagram of the CCN mechanism. a–e) Reproduced with permission.[70] Copyright 2021, Wiley-VCH. Schematic illustration of the f) invert-structured and g) normal-structured narrowband PDs. Specific detectivity spectra of the h) red PD and i) UV PD. Schematic illustration of the optical field distribution and the carrier transport in j,k) invert-structured device and l,m) normal-structured device. f-m) Reproduced with permission.[71] Copyright 2020, Wiley-VCH.

electrons and holes can be extracted efficiently. Thus, the invert-structured device realized the narrowband response in the red region. For the normal-structured device, electrons and holes excited by ultraviolet (UV) lights can be efficiently collected due to short transport paths and high hole mobility, as displayed in Figure 4l,m. In contrast, the electrons excited by red lights suffered from long transport paths and low electron mobility. Hence, the normal-structured device obtained a narrowband response in the UV region.

3.1.2. Bandpass Filters or Optical Microcavity

Combining broadband perovskite PDs with bandpass filters or an optical microcavity represents another strategy for constructing narrowband PDs.[57,58] Due to strong light absorption characteristics, perovskite materials can be used as both photosensitive layers and bandpass filters. The scheme adopting perovskite as a bandpass filter was first put forward by Li et al.[58] As shown in **Figure 5**a, the front side of the transparent glass substrate is a broadband photodiode with perovskite-2 as the photosensitive layer, and the back side is the perovskite-1 layer as a bandpass filter. The perovskite-1 filter layer was described as an optically-active-but-electronically-dead (OAED) layer, which absorbed light in the short-wavelength range but did not contribute photocurrents, as shown in Figure 5b. Actually, the part of perovskite films near the incident light in the traditional CCN-type narrowband PDs could also be called the OAED layer, as illustrated in Figure 5c, which deteriorated device performances, such as response speed, due to the increase of carrier transmission distance and the introduction of additional recombination center.[71] Therefore, separating the OAED layer from the photosensitive layer could improve device performance. The narrowband PDs were obtained by selecting suitable perovskite-1 and perovskite-2, as presented in Figure 5d. The best narrowband PDs exhibited a spectral response with an FWHM of 28 nm and a maximal SRR greater than 1000. Subsequently, Qiao et al. reported the self-powered perovskite narrowband PDs by introducing bandpass filters.[73] By adjusting the materials' bandgap of the photoactive layer and OAED layer and controlling their thickness, a series of narrowband PDs were demonstrated with spectral responses ranging from the visible to the near-infrared (NIR) region. Besides, these devices presented a narrow spectral response with an FWHM of < 50 nm and a maximal SRR of more than 1100.

Optical microcavity as an emerging filter has been applied in perovskite narrowband PDs. The optical microcavity integrated into broadband PDs allows the specific transmission of target photons without using complex optical path systems. Inspired

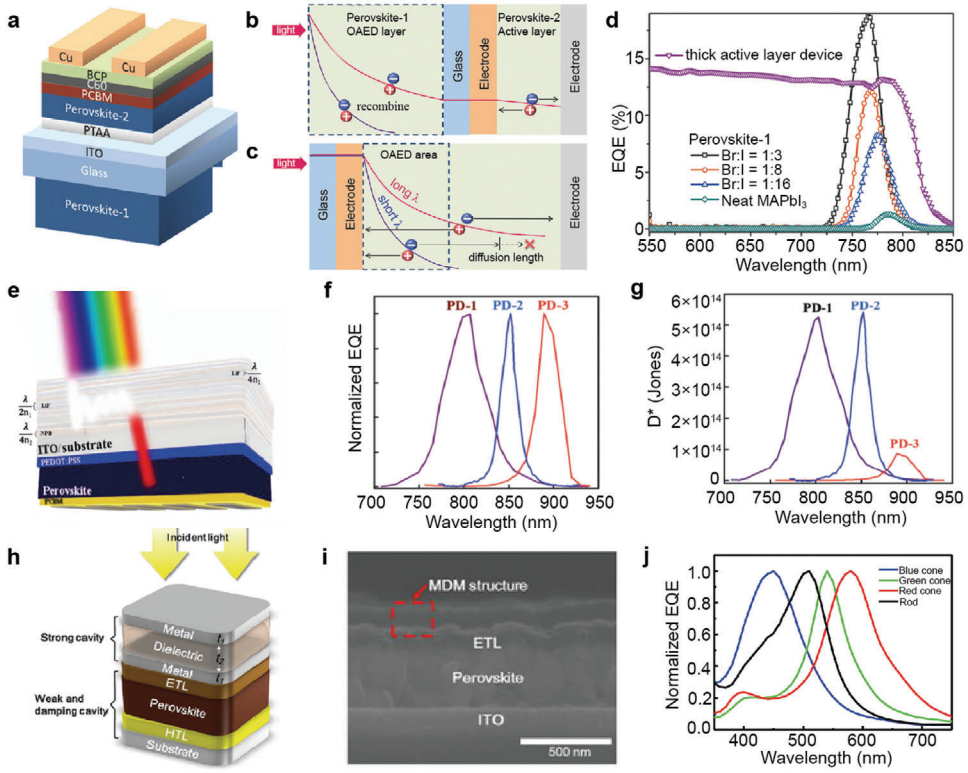

Figure 5. a) Schematically demonstrating the structure of narrowband PD with bandpass filters. Working mechanism of b) the narrowband PDs with OADE layers and c) the conventional CCN-type narrowband PDs. d) The EQE curves of narrowband PDs using different bandpass filters. a–d) Reproduced with permission.[58] Copyright 2017, Wiley-VCH. e) The structure of bionic narrowband PDs with optical microcavities. Normalized f) EQE spectra and g) detectivity of different bionic PDs. e–g) Reproduced with permission.[74] Copyright 2019, Wiley-VCH. h) Schematic structure diagram of narrowband PD with the MDM microcavity. i) Cross-sectional SEM image of the device. j) Normalized EQE spectra of narrowband PDs with different spectral responses. h–j) Reproduced with permission.[57] Copyright 2019, Wiley-VCH.

by the compound eye structure of butterflies, Cao et al. prepared bionic narrowband PDs with selective NIR photon detection by introducing optical microcavity, as illustrated in Figure 5e.[74] The optical microcavity consisted of alternating LiF (n = 1.33, n refers to refractive index)/NPB (*N*, *N*'-Bis(naphthalen-1-yl)-*N*, *N*'-bis(phenyl)benzidine, n = 2.1) layers to imitate the tapetum cells in the butterfly eyes. The peak wavelength of transmitted light could be controlled by regulating the thickness of the optical microcavity. The $CsPb_{0.5}Sn_{0.5}I_3$-based photodiodes were employed to detect NIR light in the range of ≈700–900 nm. The integrated narrowband PDs exhibited tunable narrowband response with FWHM of less than 50 nm, as demonstrated in Figure 5f. The maximal detectivity was up to 5.4×10^{14} Jones, which is superior to commercial Si-based PDs.[75,76] Another type of optical microcavity with the configuration of metal/dielectric/metal (MDM) was reported by Tsai et al., as shown in Figure 5 h,i.[57] The narrowband transmission can be designed by modulating the adopted materials and their thickness. The materials of Ag/TAPC/TmPyPB/Ag with different thicknesses were used in MDM microcavity, TAPC and TmPyPB refer to 4,4′-cyclohexylidenebis[*N*,*N*-bis(4-methylphenyl)benzenamine] and 1,3,5-tri[(3-pyridyl)-phen-3-yl]benzene, respectively. In principle, the thickness of the metal layer (t_1) and the dielectric layers (t_2) dominated the FWHM and peak wavelengths of the transmitted light, respectively. The devices prepared with perovskite PDs and MDM microcavity exhibited a tunable narrow spectral response to red, green, and blue lights, which are similar to human photoreceptors (Figure 5j).

3.1.3. Enhancement of Light Absorption in Specific Wavelengths

Narrowband PDs can also be realized by enhancing light absorption of photosensitive layers for specific spectrums. For example, the plasmonic effect was reported as a beneficial approach to regulating light harvest in constructing filterless narrowband PDs.[77,78] For the 2D Ruddlesden–Popper perovskites, the organic–inorganic periodic overlaying structure gave it natural multiple quantum wells (MQWs), leading to strong excitonic light absorptions in a narrow spectral range, as demonstrated in **Figure 6**a. Tu et al. demonstrated the function of strong exciton absorption in 2D perovskite narrowband PDs.[54] The ultrathin $(PEA)_2PbI_4$ crystals were prepared by mechanically exfoliating bulk single crystals, as shown in Figure 6b. The measurement results revealed that ultrathin $(PEA)_2PbI_4$ single crystals exhibited a narrow absorption enhancement from blue to green lights with a sharp peak at 517 nm (Figure 6c). A vertical-stacked narrowband PD with the configuration of graphene-$(PEA)_2PbI_4$-graphene was demonstrated, as shown in Figure 6d,e. The device showed a narrow spectral response with an FWHM of 15 nm and a response

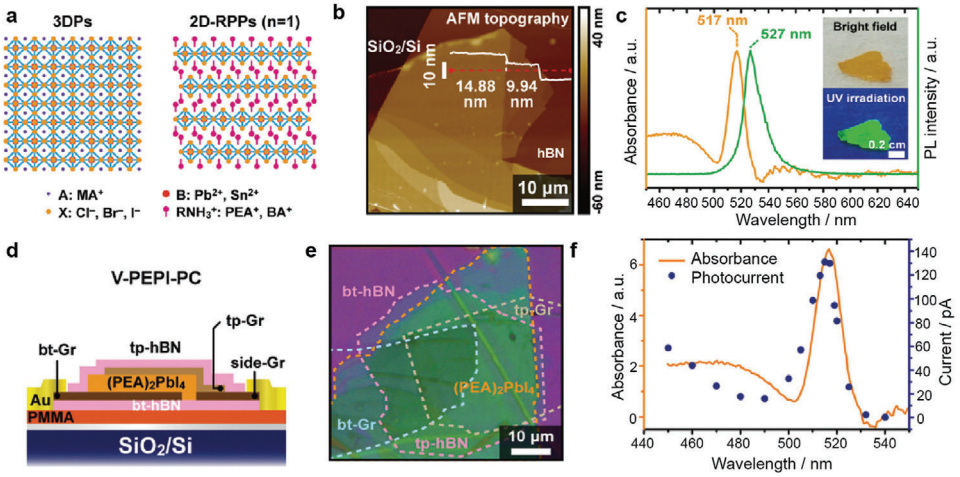

Figure 6. a) Schematically illustration of the structure of 3D and 2D perovskites. b) The AFM image of ultrathin $(PEA)_2PbI_4$ perovskites. c) The absorption spectra and PL spectra of ultrathin $(PEA)_2PbI_4$ perovskites. d) Schematic demonstration of the narrowband PD structure. e) The optical microscopic image of the device. f) The absorption spectra of ultrathin $(PEA)_2PbI_4$ perovskites and the photocurrent of the device versus wavelengths. a–f) Reproduced with permission.[54] Copyright 2020, Wiley-VCH.

peak at 517 nm, which is consistent with the exciton absorption range in ultrathin $(PEA)_2PbI_4$ crystals (Figure 6f).

3.2. Dual-Band Perovskite PDs

Different from narrowband PDs with spectral responses in a narrow range, wavelength-selective dual-band PDs have two distinct spectral response peaks in two-band regimes. The following section will review the recently reported wavelength-selective dual-band perovskite PDs. The main realization strategies include the preparation of heterojunction with different bandgap materials and the modulation by working voltages.[79,80] The detection bands of wavelength-selective dual-band perovskite PDs can be classified into visible–visible, visible–NIR, and visible–UV.[4,81,82]

3.2.1. Visible–Visible

Owing to the broad absorption of perovskite in visible, the perovskite-based PDs mainly work in either broadband or narrowband modes. The fabrication of dual-band perovskite PDs with wavelength selectivity in the visible region is difficult. The researchers are exploring in terms of new device structures and working mechanisms. Wang and co-authors synthesized centimeter-sized 2D perovskite heterostructures of $(BA)_2PbI_4/(BA)_2MAPb_2I_7$ and assembled dual-band PDs with wavelength selectivity in the visible region.[39] Due to the self-trapping states of the 2D perovskites, the device had narrow dual-band spectral responses with peaks of 540 and 610 nm and the corresponding FWHM of 20 and 30 nm, respectively. Afterward, Wang et al. reported self-driven dual-band perovskite PDs and proposed a new mechanism of charge separation reversion (CSR).[80] **Figure 7**a schematically presents the device structure, which is composed of a photovoltaic structure of FTO (fluorine–doped tin oxide)/$MAPbBr_3$/PCBM (phenyl–C61–butyric acid methyl ester)/PPDIN6 (amino-functionalized perylene diimide polymer)/Ag. The device exhibited a negative broadband response above-bandgap absorption region and a positive narrowband response in the sub-bandgap absorption region, respectively (Figure 7b). Figure 7c–e shows the schematic diagram of the CSR mechanism, revealing that the dual-band responses originate from the formation of the S-shape band structure and the thickness-related light absorption of the active layer. As sketched in Figure 7c, the S-shape band structure was formed in the perovskite layer after equilibrium due to the ion redistribution. According to Beer–Lambert law, charge carriers generated by above-bandgap photons were close to the interface of FTO/perovskite (Figure 7d). Because the photon energy ($h\nu$) is much larger than the perovskite bandgap (Eg), the excited electrons with excess energy ($h\nu$-Eg) can easily tunnel through the Schottky junction between perovskite and FTO and drifted to the FTO electrode under the action of built-in electric field, leading to a negative photoresponse. However, the sub-bandgap photons with immense penetration depth can excite the charge carriers near the PCBM side (Figure 7e). The electrons near the FTO electrode cannot pass through the Schottky junction because they have no excess energy. Thus, these photogenerated carriers were recombined by the defect states and did not contribute to the photocurrent. Meanwhile, due to the energy difference between perovskite and PCBM, the photoexcited electrons close to PCBM drifted toward the Ag electrodes, resulting in a positive photoresponse. Similarly, the voltage-modulated dual-band PDs with stacking two perovskite photodiodes in opposite polarity was reported by Huang and co-workers.[83] By modulating the direction of the driving voltage, the response of a single device could be switched between the wavelength range of 300–570 and 630–800 nm.

3.2.2. Visible–NIR

Dual-band PDs with a detection selection in visible and NIR regions have essential applications in bionic vision for daylight

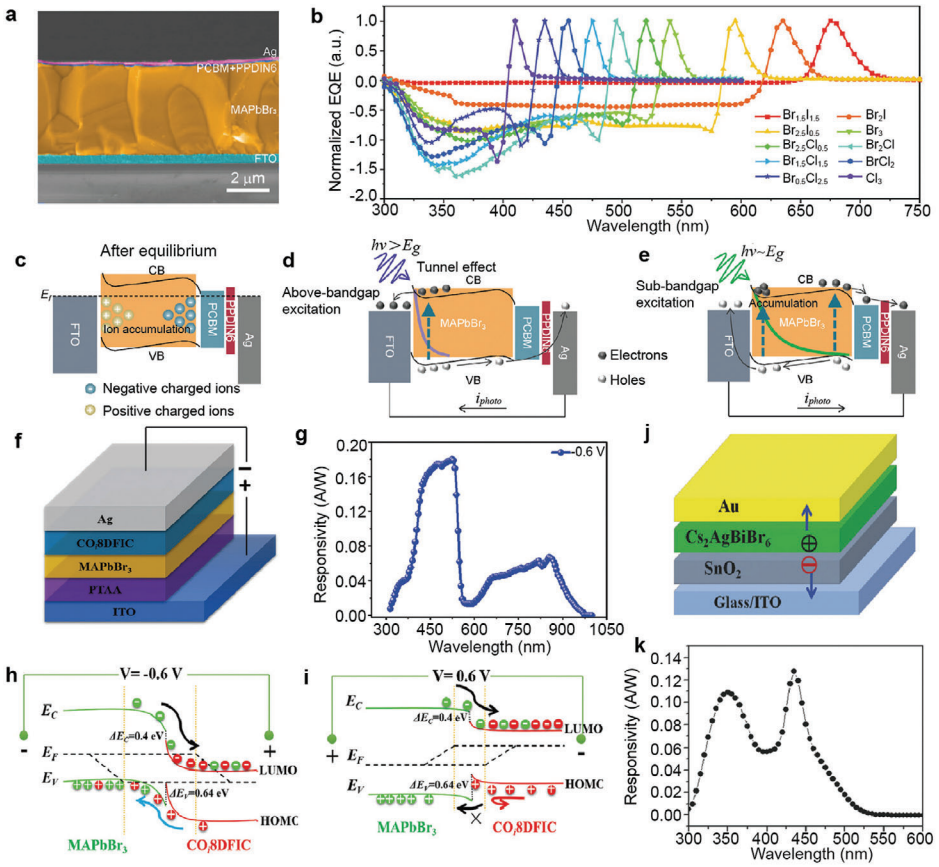

Figure 7. a) The cross-sectional SEM image of dual-band PDs with two wavelength response peaks in the visible region. b) Normalized EQE spectra of PDs prepared from perovskites with different halides. c–e) Schematic demonstration of the working principle. a–e) Reproduced with permission.[80] Copyright 2021, Wiley-VCH. f) Schematic diagram of the dual-band PDs with response peaks in the NIR and visible regions. g) The responsivity of the device under a bias of −0.6 V. h,i) The schematic energy band diagrams for the device under −0.6 and 0.6 V. f–i) Reproduced with permission.[87] Copyright 2020, Wiley-VCH. j) Schematically demonstrating the structure of dual-band PDs with response peaks in the UV and visible regions. k) The responsivity curve of the device versus wavelengths. j,k) Reproduced with permission.[79] Copyright 2020, Wiley-VCH.

visualization and night vision detection.[84,85] Organic semiconductors have been used as a cost-effective material for dual-band PDs to identify visible and NIR lights.[86] The combination of perovskite and organic materials can make up for the deficiency of organic materials in the construction of high-performance PDs. Li et al. reported dual-band PDs using nonoverlapping absorption materials of small organic molecules (CO_i8DFIC) and $CH_3NH_3PbBr_3$ films, as shown in Figure 7f.[87] This device exhibited two distinct response peaks on the condition of no power supply or the reverse bias. Figure 7g shows the spectral response of the device under a reverse bias of −0.6 V, presenting two cut-off wavelengths locate at around 544 and 920 nm, respectively. The spectral response of the device can be switched between dual-band to single-band by adjusting the operating voltages. As shown in Figure 7h, under a reverse bias (−0.6 V), the direction of the applied electric field was consistent with the built-in electric field. The energy band of CO_i8DFIC shifted downward relative to $CH_3NH_3PbBr_3$ perovskite, resulting in an increase in the responsivity compared to the device at zero voltage. In contrast, when a forward bias was applied, the direction of the applied electric field was opposite to the built-in electric field, and the energy band of CO_i8DFIC shifted upward (Figure 7i). With the increased applied electric field, the separation efficiency of excitons in $CH_3NH_3PbBr_3$ and CO_i8DFIC decreased. At 0.6 V, the excitons in CO_i8DFIC cannot be separated due to low electric field intensity and the offset of the valence band, which resulted in a single-band spectral response (visible range). Subsequently, Gao et al. also employed a similar strategy of voltage-modulated spectral response to assemble dual-band PDs.[82] The dual-band PDs with spectral response in visible and NIR regions were prepared based on $Cs_{0.15}FA_{0.85}PbI_3$ (FA refers to $CH(NH_2)_2$) and organic material (PBDBT-DTBT and BTP-4F). The bias-tunable responses were determined by energy band bending and bias-related carrier injection behaviors. This device exhibited a visible response at forward bias and a NIR response at the opposite bias, with responsivities of 93.5 and 102.2 mA W^{-1}, respectively.

3.2.3. Visible–UV

Dual-band PDs capable of recognizing visible and UV lights have aroused attractive applications in secure communication, chemical analysis, and environmental monitoring.[81] The perovskite materials combined with traditional UV semiconductor

materials, such as SnO_2, ZnO, and GaN, represent a simple and effective approach for fabricating visible–UV dual-band PDs.[79,88] Wu et al. reported visible–UV dual-band PDs using $Cs_2AgBiBr_6/SnO_2$ heterojunction, as shown in Figure 7j.[79] This device had two distinct spectral response peaks at 350 and 435 nm, respectively (Figure 7k). A high response of 0.11 A W^{-1} was obtained at 350 nm with a rapid response time of less than 3 ms, which is significantly higher than other UV PDs based on semiconductor oxide heterojunction. The majority of reported dual-band PDs based on heterojunctions were implemented by complex manufacturing processes, which inevitably imported defects in the depletion layer. Recently, Fang et al. reported dual-band PDs by using $Cs_3Bi_2Br_9/Cs_3BiBr_6$ perovskite bulk heterojunction.[89] The device presented two spectral response peaks located at 360 and 450 nm, with responsivities of 59.4 and 3.09 mA W^{-1}, respectively. Remarkably, this device exhibited excellent optoelectronic performances in the UV band, including high detectivity of 1.2×10^{12} Jones, a high on/off current ratio of 18 881, and a fast response speed (rise and fall times: 1.4 and 2 μs), respectively.

3.3. Multispectral-Recognizable Perovskite PDs

Multispectral recognition refers to distinguishing photon signals with two and more ranges of wavelength. Commercial multispectral PDs rely on complicated optical elements, e.g., prisms, interferometric filters, and diffraction grating, which hampers their development to miniaturization and integration.[90,91] The multispectral-recognizable perovskite PDs could achieve wavelength-selective response over a wide spectral range without the need for a dispersion element.[25] By simply varying the halide ions (I^-, Br^-, Cl^-) and the organic ions (methylammonium [MA^+] or formamidinium [FA^+]), a multitude of perovskites with customized bandgap can be available.[92] To fully realize this concept, two promising fabrication strategies are proposed for high-performance multispectral detectors, including integrating different bandgap perovskite materials on the same substrate and using gradient bandgap-tunable perovskite materials.[93,94]

3.3.1. Integrating Different Bandgap Perovskite Materials on the Same Substrate

Integrating different bandgap perovskite materials on the same substrate is an inevitable way to fabricate PDs with a selective spectral response. Schröder et al. prepared different compositional perovskite films with an absorption cutoff from 410 to 790 nm by combinatorial inkjet printing method (**Figure 8**a,b).[94] The tunability of absorption cutoff achieved an 8 nm step for $MAPb(BrxCl_{1-x})_3$ compositions by shifting the bandgap with fine-tuned ink ratio. The PDs fabricated using different compositional perovskite films exhibited spectral response corresponding to the respective bandgap (Figure 8b). Meanwhile, a distinct photoresponse matrix with spectral selectivity was obtained using light sources with different wavelengths to irradiate the PDs along the perovskite gradient, as shown in Figure 8c. Chen et al. fabricated PD arrays by integrating three PDs with different perovskite components in each cell (Figure 8d).[95] In this report, an improved evaporation method was developed to boost the crystal quality of halide perovskite films, in which the substrates were treated with a self-assembled monolayer. Figure 8e displays the image of the compact $CsPbBr_3$ films with larger crystalline grains. The perovskites of $CsPbI_2Br$, $CsPbBr_3$, and $CsPbBrCl_2$ with optical bandgaps of 1.91, 2.33, and 2.75 eV were employed as active materials (Figure 8f). The spectral response for the $CsPbI_2Br$, $CsPbBr_3$, and $CsPbBrCl_2$ PDs was displayed in Figure 8g, revealing the fabricated PD arrays can discriminate red, green, and blue lights. Furthermore, to achieve spectral recognition together with high resolution, Wang et al. constructed flexible full-color PD arrays by fabricating various bandgap perovskite films on the same substrate via electrohydrodynamic printing of ionic-liquid-based ink (Figure 8h,i).[96] By optimizing the printing conditions, the perovskite dot arrays with an extremely high resolution of 1 μm (5070 dpi) were successfully prepared. Simultaneously, the as-fabricated demonstrated the potential in color imaging, as shown in Figure 8j.

3.3.2. Using Gradient Bandgap-Tunable Perovskite Materials

Using gradient bandgap perovskite materials to assemble PDs with a continuously tunable photoresponse is an advanced technique that can precisely recognize the visible spectrum. A light signal in different spectral regions can be discriminatively collected to project the hue information that best represents the color. The more signals from different spectral regions, the higher the hue resolution is. Inspired by this, Zhang et al. developed rainbow perovskite films prepared by a halide-exchanging method as the active layer of the PDs for intensity and color perception, as shown in **Figure 9**a,b.[93] The device consists of two parts (Figure 9c): one is a photoactive layer composed of perovskite films with a relatively small bandgap (SBG), and the output current (I^{SBG}) shows linear response to the total photon flux (ϕ) in a certain photon energy (ϵ) region; the other is a photosensing layer consisting of semiconductors (dioctylbenzothieno [2,3-b] benzothiophene and rainbow perovskites) with gradient bandgap (GBG). The photogenerated current output (I_{ph}^{GBG}) relates to the average photon energy ($\overline{\epsilon_\phi}$) that and photon flux (ϕ). For nonmonochromatic light, the I_{ph}^{GBG} can be expressed as[93]

$$I_{ph}^{GBG} \propto \left(\overline{\epsilon_\phi} - \epsilon_0\right)\phi \tag{10}$$

where ϵ_0 is the smallest bandgap of the GBG film employed in the device, and the ($\overline{\epsilon_\phi}$) is weighted by the flux $\overline{\epsilon_\phi} = p/\phi$, p is the total power density. Hence, by combining two signals generated from two parts of the device, the intensity and color information (hue, represented by $\overline{\epsilon_\phi}$) of the tested spectrum can be obtained. Figure 9d summarized the spectral information derived from the fabricated PDs, which are in good agreement with those obtained from a commercial spectrometer.

Furthermore, gradient bandgap-tunable perovskite materials can be applied for miniature on-chip spectrometers with the assistance of a computing algorithm, as schematically in Figure 9e.[97] The tunable response range of PDs based on gradient bandgap perovskite materials sets the precondition for computational spectral recognition. Sun et al. prepared filterless wavelength-sensitive PDs based on the gradient bandgap-tunable

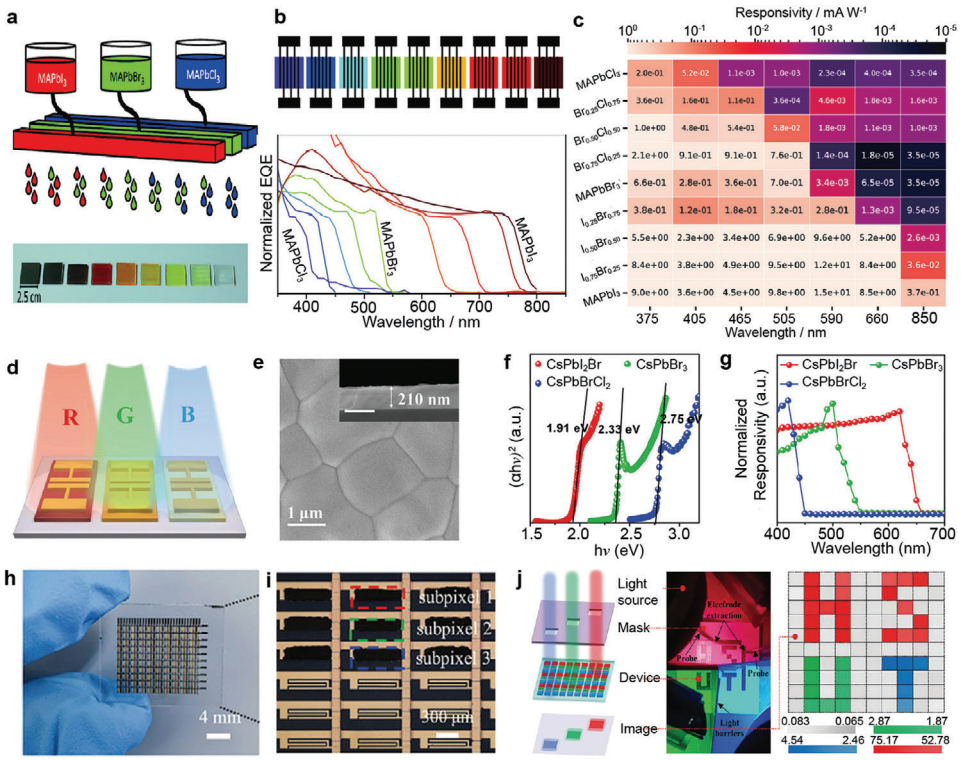

Figure 8. a) Schematic illustration of the combinatorial inkjet printing approach and the photograph of synthesized perovskite films. b) The normalized EQE spectra of the PDs fabricated with gradient composition perovskites. c) A matrix of responsivities obtained with gradient response PDs. a–c) Reproduced with permission.[94] Copyright 2021, Wiley-VCH. d) Schematic illustration of multicomponent perovskite PDs. e) The SEM image of $CsPbBr_3$ films synthesized by an improved evaporation method. f) The optical bandgap of $CsPbI_2Br$, $CsPbBr_3$, and $CsPbBrCl_2$ films. g) The normalized responsivity of PDs prepared with $CsPbI_2Br$, $CsPbBr_3$, and $CsPbBrCl_2$ films. d–g) Reproduced with permission.[95] Copyright 2021, Wiley-VCH. h,i) The photographs of PD arrays in which each pixel contains three sub-pixel pixels. j) The imaging results and schematic diagram of the imaging test set-up. h-j) Reproduced with permission.[96] Copyright 2021, Wiley-VCH.

perovskite of $KMAPbCl_xBr_{3-x}$. These materials with the absorption edge evolving from 450 to 780 nm formed by repeating spin-coating MACl precursor and annealing process (Figure 9f,g).[97] The device exhibited the maximum EQE of over 90% and an ultrafast speed with a response time down to 71 ns, which was impacted by the junction capacitance via electron-donor control (Figure 9h). More importantly, a spectral resolution of ≈80 nm can be well realized by integrating six pixels in the different positions of devices. Subsequently, Zeng et al. reported a miniaturized multispectral detector without delicate optical elements based on gradient bandgap $MAPbX_3$ microwires with a length of 4 mm, in which halide ions varied from Cl to I along the axis (Figure 9i).[40] Figure 9j shows the fluorescence spectra at different positions of the microwires. Gradient bandgap-tunable microwires enabled the spectral detector to a response range covering 450–790 nm, as presented in Figure 9k. More importantly, the miniaturized detectors presented the capacity of multispectral sensing with a relatively higher resolution of 25 nm.

3.4. X-Ray Perovskite PDs

X-ray detectors have a wide range of applications in daily life and industrial production, including nondestructive tests, medical diagnosis, security inspection, etc.[98] In addition to the common detection of UV, visible, and NIR lights, the metal perovskite materials have revolutionized the field of radiation detection, especially in X-ray detection.[30] The advantages of halide perovskite in optical, electrical, and structural aspects endow it as the most promising material for assembling X-ray detectors, which are summarized as follows:[22] 1) the heavy atom compositions, such as Pb, Br, and I atoms; 2) high photoluminescence yield and wide color gamut; 3) decent carrier mobility, long carrier lifetime, and low trap density; 4) simple and low-cost synthesis process. Up to now, numerous works have been carried out on perovskite-based X-ray detectors, which can be divided into direct-conversion X-ray detectors and indirect-conversion X-ray detectors (perovskite materials as scintillators) according to the detection mode.[34,99]

3.4.1. Direct-Conversion X-Ray Detector

The direct-conversion X-ray detectors work based on the photoelectric effect, in which photons of X-ray radiation are absorbed by perovskites to generate photocurrents.[100] This type of X-ray detector has several unique advantages, including fast response speed, wide linear response range, and high-energy resolution.[101] In recent years, many achievements have been made in terms of X-ray sensitivity, flexibility, and resolution. Huang et al. reported an ultrasensitive X-ray detector with a

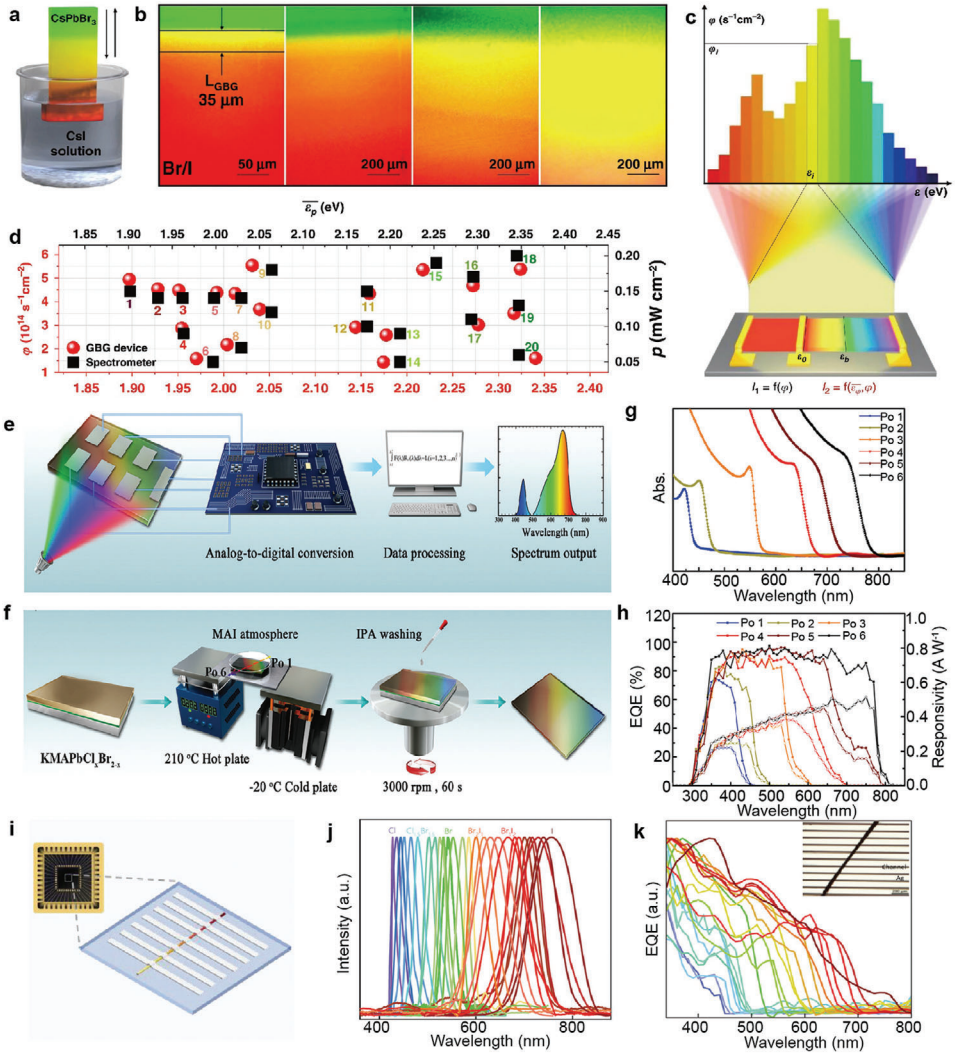

Figure 9. a) Schematic demonstration of the halide-exchanging method for preparing bandgap-gradient perovskite films. b) Fluorescence microscopy images of Br/I perovskite films. c) Conceptual demonstration of wavelength perception using the fabricated spectrometer. d) The $\overline{\varepsilon_\phi}$ values measured by the GBG device and spectrometer. a–d) Reproduced with permission.[93] Copyright 2020, Springer Nature. e) Schematic illustration of spectral recognition using wavelength-sensitive PDs combinate with the algorithm. f) The preparation process for gradient bandgap-tunable $KMAPbCl_xBr_{3-x}$ perovskites. g) Absorption spectra of six positions in $KMAPbCl_xBr_{3-x}$ perovskite films. h) The EQE curves at different points in the device. e–h) Reproduced with permission.[97] Copyright 2020, Wiley-VCH. i) Schematic diagram of the gradient perovskite microwire PD arrays. j) The PL spectra of gradient $MAPbX_3$ microwire. k) The EQE curves of PDs prepared on different positions of the $MAPbX_3$ microwire. i-k) Reproduced with permission.[40] Copyright 2022, Wiley-VCH.

sensitivity of 2.1×10^4 μC mGy_{air}^{-1} cm^{-2} under X-ray radiation of 8 keV by integrating $MAPbBr_3$ single crystals on Si substrates, which is over a thousand times higher than the sensitivity of the reported α-Se X-ray detectors.[102] And a flexible direct-conversion X-ray detector array has also been demonstrated for realizing X-ray imaging on a curved surface, in which a perovskite-filled membrane was prepared as an active layer with good flexibility and stability.[103] This device can stably work at a radius down to 2 mm. Kim et al. reported a flat-panel X-ray imager with high resolution by combining polycrystalline hybrid perovskite films with TFT arrays.[104] The active layer with the configuration of polyimide-perovskite composites/thick perovskite films/polyimide-perovskite composites was printed onto the TFT backplane. The modulation transfer function (MTF) representing the spatial resolution was 0.2 at 3.1 lp mm^{-1} for the flat-panel X-ray detector superior to the α-Se X-ray detectors.[105] According to a similar strategy, Xia et al. synthesized compact and large-area perovskite films by soft-pressing methods incorporating polymerizable binder and obtained the state-of-the-art direct-conversion flat-panel X-ray imager among polycrystalline films, with a ratio of sensitivity to noise current up to 1.41×10^{11} μC Gy^{-1} A^{-1} (**Figure 10**a–c).[106] Recently, Zhan et al. reported robust 120 keV direct-conversion hard X-ray detectors based on as-grown single crystal of $CsPbBr_{3-n}X_n$ (X = Cl, I) (Figure 10d).[107] Figure 10e shows the time-dependent response of $CsPbBr_3$, $CsPbBr_{2.9}I_{0.1}$, and CdZnTe X-ray detectors at different electric field intensities, demonstrating that $CsPbBr_{2.9}I_{0.1}$ X-ray detectors have respectable response stability

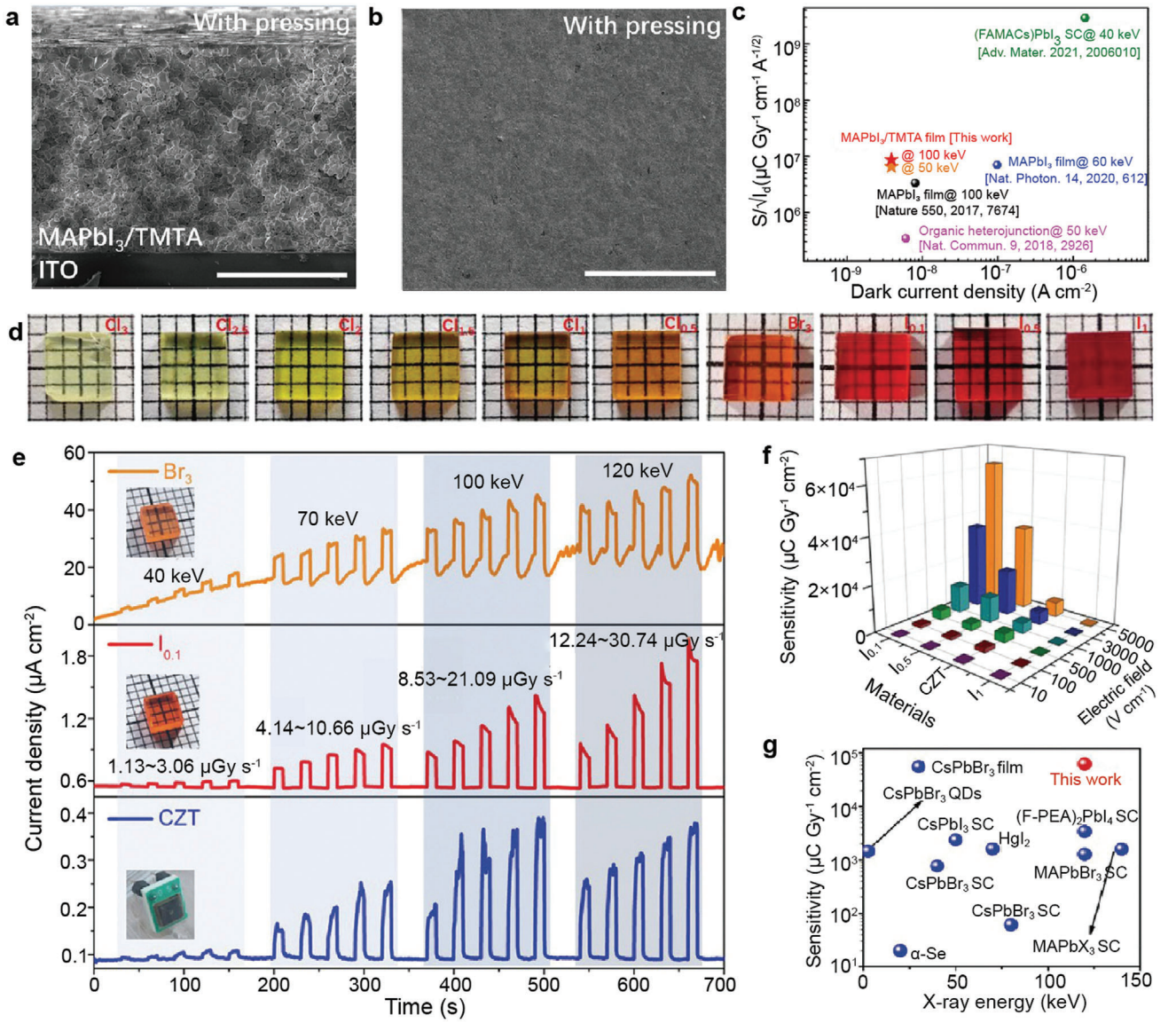

Figure 10. a) Cross-sectional SEM image of the thick $MAPbI_3$/TMTA films. scale bar: 100 μm. b) The surface SEM image of thick $MAPbI_3$/TMTA films. scale bar: 20 μm. c) Summary of dark current and the ratio of sensitivity to noise current for X-ray perovskite detectors. a–c) Reproduced with permission.[106] Copyright 2022, Wiley-VCH. d) The photographs of $CsPbBr_{3-n}I_n$ single crystals. e) The *I–t* curves of $CsPbBr_3$, $CsPbBr_{2.9}I_{0.1}$, and CdZnTe X-ray detectors. f) Sensitivity of $CsPbBr_{3-n}I_n$ (n = 0.1, 0.5, and 1) and CdZnTe X-ray detectors. g) Comparison of the sensitivity for different X-ray detectors. d–g) Reproduced with permission.[107] Copyright 2022, Wiley-VCH.

under high electric field, which is comparable to CdZnTe X-ray detectors.[108] A record sensitivity of 6.3×10^4 μC Gy^{-1} cm^{-2} and a low detection limit of 54 nGy s^{-1} for the 120 keV hard X-ray detection were achieved by $CsPbBr_{2.9}I_{0.1}$ and $CsPbBr_2I$ X-ray detectors, respectively (Figure 10f,g).

3.4.2. Indirect-Conversion X-Ray Detector

The indirect-conversion X-ray detector consisted of a scintillator that converts high-energy X-ray into visible or UV lights and a conventional photosensor, such as complementary metal-oxide semiconductor (CMOS) detectors and charge-coupled devices (CCD), to capture the converted lights.[109] Compared with direct-conversion X-ray detectors, indirect-conversion X-ray detectors possess characteristics of stability, low cost, and easier integration with commercially electronic components (CMOS or TFT arrays), which is the mainstream approach in X-ray detection.[22] Perovskite materials, including bulk single crystals, nanowire single crystals, and polycrystalline films have been proven to be excellent scintillators.[14] Birowosuto et al. reported the bulk perovskite single crystal of $CH_3NH_3PbI_3$ and $CH_3NH_3PbBr_3$ as scintillators (**Figure 11**a).[34] The X-ray radioluminescence (RL) spectra (light color area) of $MAPbI_3$ and $MAPbBr_3$ were in accord with their photoluminescence spectra (dark color area), as shown in Figure 11b,c. And both perovskite single

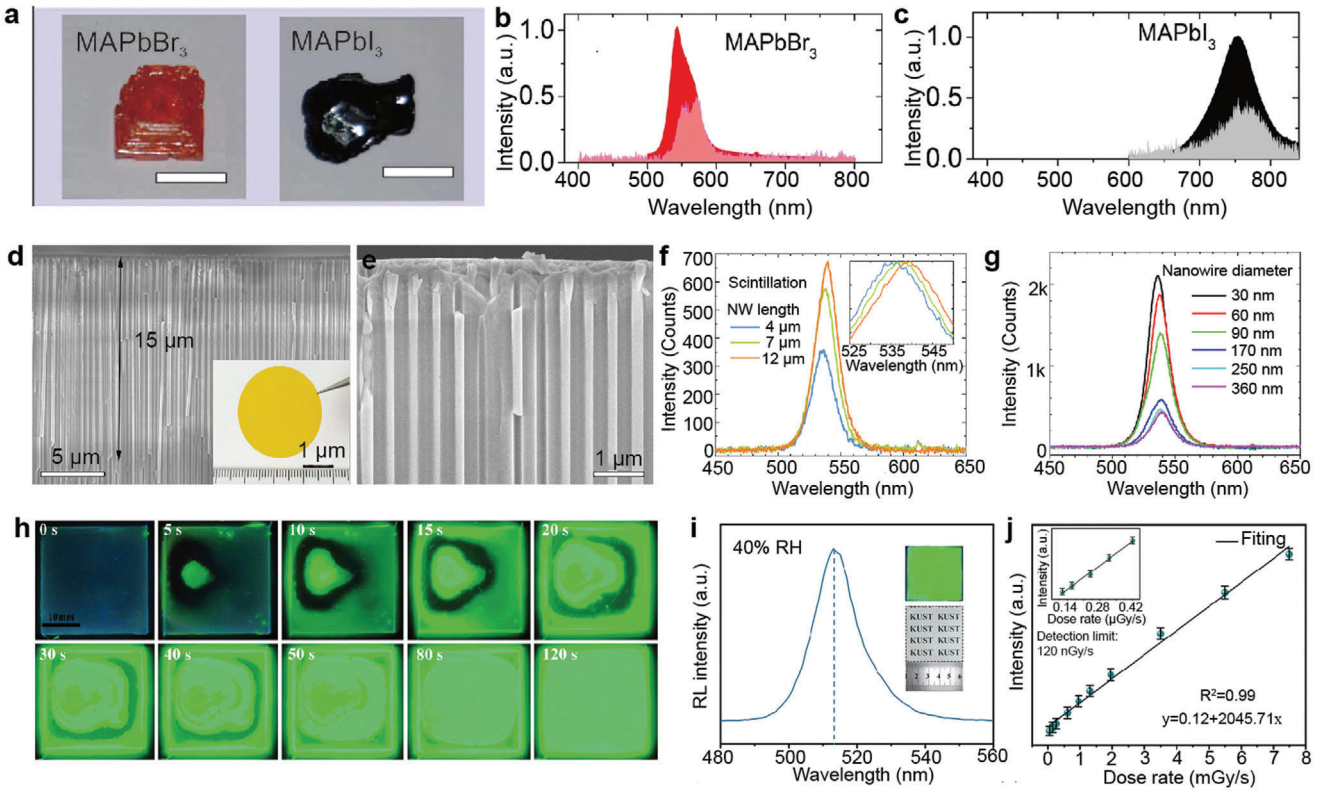

Figure 11. a) The photographs of $MAPbBr_3$ and $MAPbI_3$ single crystals. b,c) The PL and RL spectra of $MAPbBr_3$ and $MAPbI_3$ single crystals. a-c) Reproduced with permission.[34] Copyright 2022, Springer Nature. d,e) Cross-sectional SEM images of $CsPbBr_3$ nanowires synthesized in AAO templates. The RL intensity versus the f) nanowire length and g) nanowire diameter. d–g) Reproduced with permission.[110] Copyright 2021, American Chemical Society. h) Photographs of the $CsPbBr_3$/PMMA films on an 80 °C hotplate recorded under UV illumination. i) The RL spectrum of $CsPbBr_3$/PMMA films at a 40% humidity environment. j) The RL intensity versus dose rate of X-ray. h–j) Reproduced with permission.[111] Copyright 2021, Wiley-VCH.

crystals have high luminescence yields of over 120 000 photons MeV^{-1} from the X-ray excitation at low temperatures (T = 130 K). Zhang et al. reported stable scintillators of $CsPbBr_3$ single-crystalline nanowires, achieving a micrometer-scale ultrahigh spatial resolution.[110] The $CsPbBr_3$ nanowires with diameters ranging from 30 to 360 nm were grown in anodized aluminum oxide (AAO) membrane template (Figure 11d,e). The RL intensity of this scintillator increased as the length increased and the diameter decreased of perovskite nanowires, respectively (Figure 10f,g). The scintillator with perovskite nanowires of 30 nm diameter harvested the maximum luminescence yield of 5300 photons MeV^{-1}. Because the perovskite nanowires were encapsulated in the AAO template, the RL intensity of the scintillation was not degraded after two months in the ambient environment, demonstrating high environmental stability. Chen et al. prepared a flexible and refreshable scintillator based on the perovskite polycrystalline films, which was defined as a perovskite "polymer-ceramics" scintillator with $CsPbBr_3$ nanocrystals growing in the polymethylmethacrylate (PMMA) polymer.[111] Figure 11h displays the photoluminescence images of fresh $CsPbBr_3$-PMMA films in the crystallization process, indicating that perovskite crystals are uniformly dispersed into PMMA polymer. Under the excitation of X-ray radiation, this scintillator exhibited robust RL at a 40% humidity environment (Figure 11i). Moreover, RL intensity presented a function on incident X-ray dose rate and this indirect-conversion X-ray detector realized a detection limit of 120 nGy s^{-1}, as shown in Figure 11j.

4. Applications of Wavelength-Selective Perovskite PDs in Image Sensing

The wavelength-selective PDs not only respond to the light intensity but also can recognize light wavelengths, which plays a crucial role in image sensing. This section summarizes the applications of wavelength-selective perovskite PDs in image sensing. One way of image sensing is based on multipixel image sensors, where each PD acts as a pixel to convert optical signals into electrical signals.[56] All the electrical signals are collected and then processed by software to reconstruct the original 2D images. Another way of image sensing is achieved by a single-pixel PD, that is, single-pixel imaging.[70] The PDs collect optical signals from different positions in the 2D image by moving along the *x*-*y* biaxial. This way takes a long time to reconstruct a clear image and cannot realize dynamic imaging. As a consequence, single-pixel imaging is only utilized in the laboratory as a strategy to validate the PD's imaging potential. According to the spectral recognition capability of wavelength-selective perovskite PDs, image sensing can be mainly divided into single-/dual-color imaging, multicolor imaging, and X-ray imaging.[40,87,112]

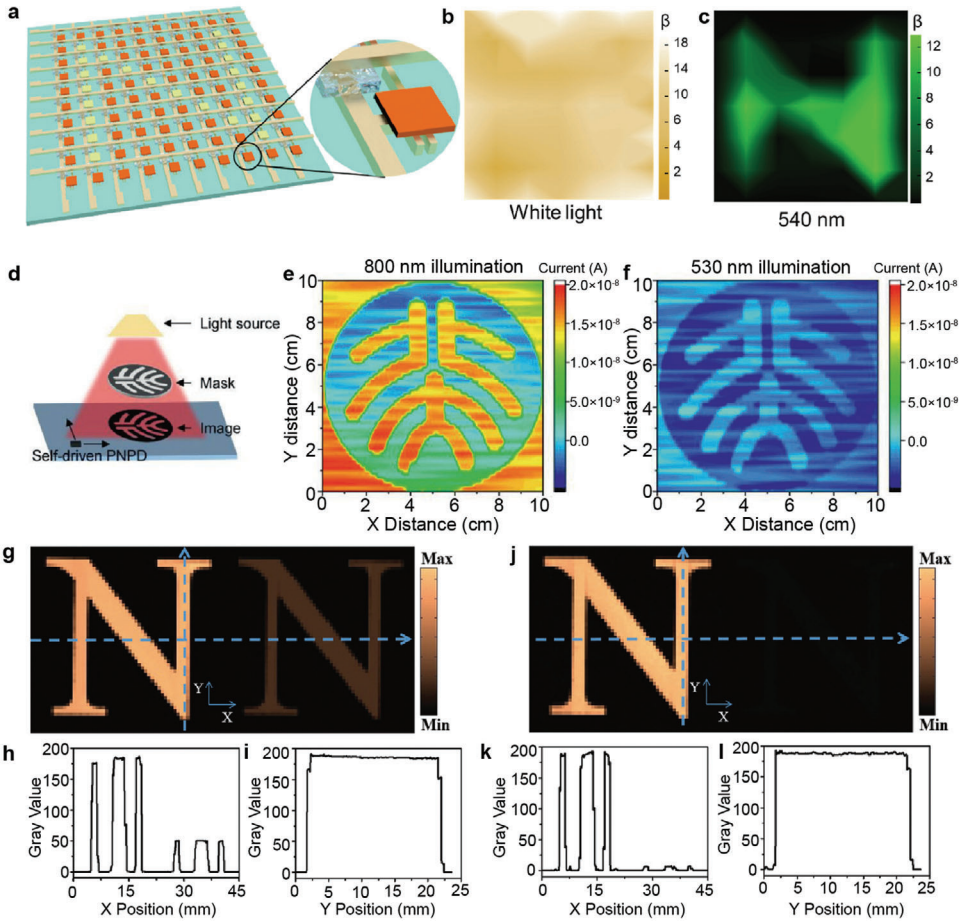

Figure 12. a) The structure of CCN-type narrowband PD arrays. The imaging results of the device under b) white light and c) 540 nm light illumination. a–c) Reproduced with permission.[56] Copyright 2018, American Chemical Society. d) Schematic diagram of single-pixel imaging for self-driven narrowband PDs. The imaging results of the device under e) 800 nm light and f) 530 nm light illumination. d–f) Reproduced with permission.[70] Copyright 2020, Wiley-VCH. g) Dual-color imaging results of the device at 0 V bias and the scanning currents in the h) *x*-axis direction and in i) the *y*-axis direction. j) Single-color imaging results of the device at 0.6 V bias and the scanning currents in k) the *x*-axis direction and in l) the *y*-axis direction. g–l) Reproduced with permission.[87] Copyright 2020, Wiley-VCH.

4.1. Single-/Dual-Color Imaging

Narrowband perovskite PDs with the characteristic of spectral response in a narrow range can realize single-color imaging. Xue et al. designed an image sensor by integrating 10 × 10 pixelated narrowband perovskite PDs, as schematically displayed in **Figure 12**a, where the thick perovskite films of $CsPbBr_3$ and $CsPbBr_{1.5}I_{1.5}$ were utilized for the recognition of different spectra, and the $CsPbBr_3$-based PDs were arranged in the shape of "N" letter.[56] Under the illumination of white light, all pixels can be excited, whose photocurrent values showed good consistency, and thus no discernible images appeared (Figure 12b). When monochromatic light of 540 nm was applied, a luminous letter "N" can be identified because the $CsPbBr_3$-based narrowband PD arrays were selectively activated, as shown in Figure 12c. Similarly, a legible dark letter "N" also appeared at 610 nm monochromatic light due to the selective excitation of the $CsPbBr_{1.5}I_{1.5}$-based narrowband PDs. Those results prove that these narrowband PDs achieved single-color imaging. Wang et al. demonstrated single-color imaging based on single-pixel perovskite narrowband PDs, as shown in Figure 12d.[70] The fabricated narrowband PDs with thick $MAPbI_3$ films possessed a narrow spectral response with a wavelength response peak at 800 nm and an FWHM of ≈29 nm. Under the illumination of 800 nm monochromatic light, a clear 2D image was obtained by *x*-*y* biaxial scanning with the single-pixel narrowband PDs, as presented in Figure 12e. In contrast, the observed 2D image was blurry under monochromatic light at 530 nm, which attributed to the suppression of the photoresponse in the short wavelength range (Figure 12f). Further optimization of the SRR of the device could obtain better single-color imaging results. In addition, the dual-band PDs with featuring two response peaks could realize dual-color imaging. Li et al. demonstrated dual-color imaging by self-powered dual-band perovskite PDs.[87] The imaging systems are also based on single-pixel *x*-*y* biaxial scanning. The collected current signals were converted into gray values during the image reconstruction process. At zero bias voltage, a visible/NIR image with 56 × 59 pixels was obtained, which displayed an "N" pattern with sharp boundaries under both visible and NIR regions, as shown in Figure 12g. The gray value ratio of the visible/NIR

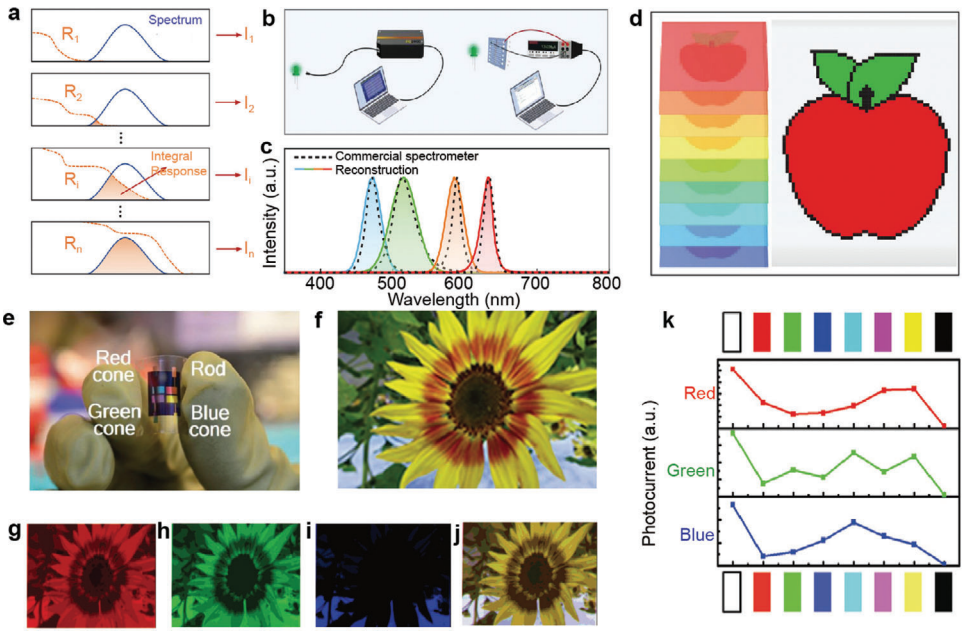

Figure 13. a) Schematic illustration of the algorithm for spectral recognition. b,c) Schematic demonstration of the spectrum detection with a commercial spectrometer and miniaturized detector, and the corresponding measurement results. d) The reconstructed images with the miniaturized detector. a-d) Reproduced with permission.[40] Copyright 2021, Wiley-VCH. e) The photograph of artificial narrowband photoreceptors. f) The original photograph of a sunflower. g–i) The scanned images with red, green, and blue narrowband PDs. j) The reconstructed image of a sunflower with the images of (g–i). k) Current signals obtained by scanning colored stripes with different PDs and the images of reconstructed colored stripes. e–k) Reproduced with permission.[57] Copyright 2019, Wiley-VCH.

image is around 3.7:1, thus this dual-color image can be recognized (Figure 12h,i). Because this device can realize the conversion of dual-band response to single-band response under voltage modulation, this device at 0.6 V bias achieved single-color imaging in the visible range, as presented in Figure 12j–l.

4.2. Full-Color Imaging

Multispectral-recognizable perovskite PDs could achieve full-color imaging. Xu et al. demonstrated full-color imaging via a multispectral PD array combined with the algorithm for spectral recognition.[40] In detail, to reconstruct the unknown spectrum F(λ), the photocurrent (I_i) of detector unit can be expressed below[113]

$$I_i = \int_{\lambda 1}^{\lambda 2} F(\lambda)\ R_i(\lambda)\,,\ i = 1, 2, 3, \ldots, n \tag{11}$$

where $\lambda_1$and λ_2 are the working wavelength range of the PD arrays, respectively, $R_i(\lambda)$ is the precalibrated response function of each device, and I_i is the measured photocurrent. Optimized calibration of spectral curves of the incident light can be recognized by adopting the adaptive regularization program to simplify computational spectral reconstruction. The algorithmic mechanism is shown in **Figure 13**a. To verify the wavelength recognition ability of the prepared miniaturized multispectral detector based on a single $MAPbX_3$ microwire, a commercial spectrometer was employed as a comparison (Figure 13b). Figure 13c shows the incident light spectra measured with a commercial spectrometer (dashed line) and reconstructed with a single $MAPbX_3$ microwire detector (solid line), indicating that the miniaturized spectral detector can symbolize the spectral region with a little worse accuracy. This miniaturized detector showed a spectral mismatch of <10 nm that still precedes the commercial spectral detector (P4M, SZ DJI Technology Co., Ltd. Spectral mismatch: 16 nm). Figure 13d displays the full-color image reconstructed by the miniaturized spectral detector, which is exactly consistent with the target picture. In addition, full-color imaging can also be realized by on-chip integration of narrowband PDs that respond to red, green, and blue lights, respectively. Tsai et al. constructed artificial human photoreceptors with four narrowband perovskite PDs, where three pixels were used as cones to detect red, green, and blue lights, respectively, and another pixel was used as rods to perceive surrounding conditions when light intensity is low (Figure 13e).[57] To demonstrate full-color imaging capabilities, a real picture of the sunflower was scanned using artificial human photoreceptors (Figure 13f). Figure 13g–i shows the images plotted with the scanning current results. Since the original image of the sunflower was dominated by red, green, and yellow colors, the red and green PDs had high signals, whereas the blue PD exhibited high signals only in the background image of the sky. The reconstructed image combining the images of Figure 13g–i with minor artifacts is presented in Figure 13j, which is highly similar to the original one. In addition, the red, green, and blue PDs were employed to simultaneously scan a series of colored stripes to further verify the spectral recognition capability. The photocurrent signals were summarized in Figure 13k. By normalization and calibration of black and white results, the reproduced colored stripes were very similar to the original stripes.

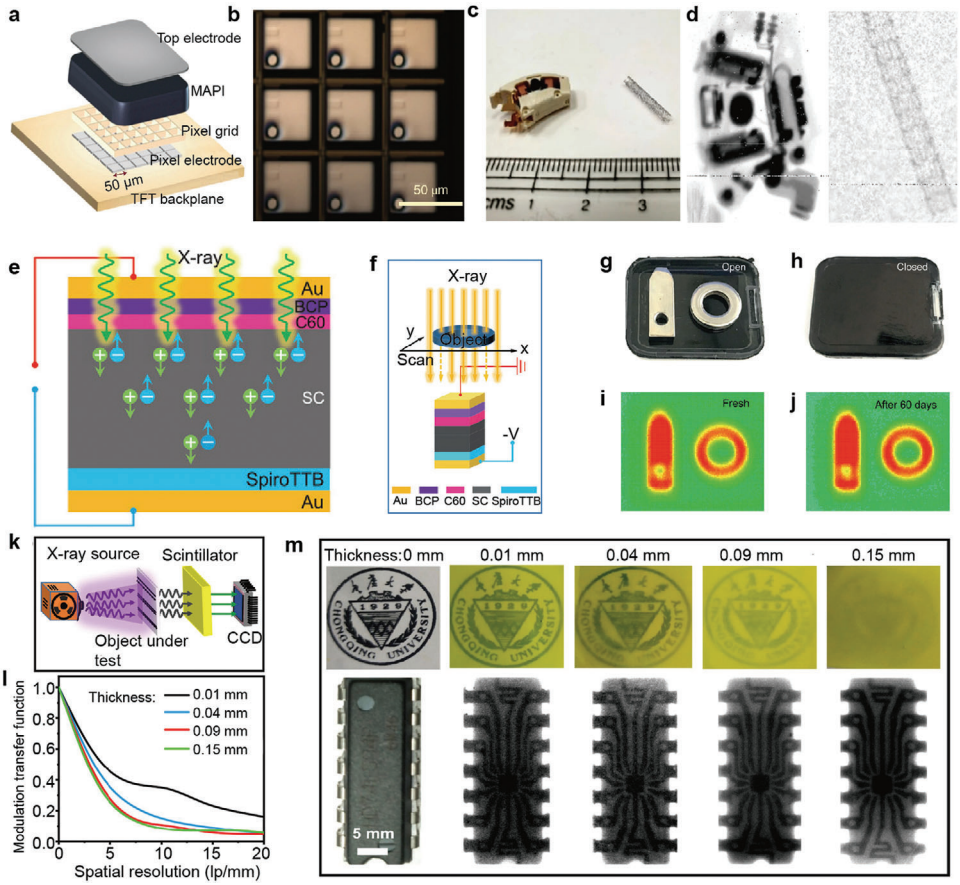

Figure 14. a) Schematic demonstration of the pixelated perovskite X-ray detector. b) Optical microscopy image of local pixels in the device. c) Photographs of part of a hearing aid and a metallic coronary stent. d) The corresponding X-ray imaging results. a–d) Reproduced with permission.[115] Copyright 2021, Springer Nature. e) Schematic illustration of the structure of a single-pixel perovskite X-ray detector. f) Schematic demonstration of single-pixel X-ray imaging. g,h) Photographs of metal objects in a plastic box. i,j) The X-ray imaging results with the X-ray detector freshly prepared and after 60 days of storing. e-j) Reproduced with permission.[116] Copyright 2021, Wiley-VCH. k) Schematic illustration of X-ray imaging using perovskite scintillator combines with CCD. l) The MTF versus spatial resolution of scintillator with different thicknesses. m) Photographs of the scintillator with different thicknesses and the corresponding X-ray imaging results. k–m) Reproduced with permission.[118] Copyright 2022, Wiley-VCH.

4.3. X-Ray Imaging

The realization of X-ray imaging based on perovskite X-ray detectors has three ways: using pixelated X-ray detectors, single-pixel X-ray detector scanning, and perovskite scintillators combined with image sensing devices.[23,104,114] Deumel et al. demonstrated high-resolution X-ray imaging by using a pixelated perovskite X-ray detector.[115] The device with 508 pixels per inch was fabricated by incorporating soft-sintered $MAPbI_3$ perovskites onto the TFT backplane (**Figure 14**a,b). The X-ray detector exhibited a high sensitivity of 9300 μC Gy_{air}^{-1} cm^{-2}, a low detection limit of 0.22 nGy_{air} per frame as well as a high spatial resolution of 6 lp mm^{-1}. To demonstrate high-resolution X-ray imaging, part of a hearing aid (diameter ≈2 mm; length ≈15 mm) and a coronary stent (cross section ≈100 × 200 μm^2) were selected as research objects, as shown in Figure 14c. Under the X-ray radiation of 4.17 μGy_{air} per frame, the obtained X-ray images provided a detailed view of the sample structure, and even the mesh structure of the coronary stent could be identified, as displayed in Figure 14d. Liu et al. reported single-pixel X-ray imaging based on triple-cation mixed-halide perovskite of $FA_{0.85}MA_{0.1}Cs_{0.05}PbI_{2.55}Br_{0.45}$, as presented in Figure 14e.[116] The X-ray detector with a photodiode-type structure exhibited high sensitivity of (3.5 ± 0.2) × 10^6 μC Gy_{air}^{-1} cm^{-2} under the 40 keV X-ray radiation, which is 29 times larger than the previously reported polycrystalline $MAPbI_3$ wafer.[117] Figure 14f displays the experimental set-up of the X-ray imaging, where a plastic box containing two metal objects was placed between the detector and the X-ray source. Figure 14i shows the clear X-ray imaging results, which correspond to the original morphology of the object hidden in the plastic box (Figure 14g,h). Remarkably, this detector with good stability was still imaging of the same plastic box after 60 days, and the radiograph same as the result produced from the fresh detector, as shown in Figure 14j. Wang et al. demonstrated X-ray imaging by combining the X-ray $CsPbBr_3$ nanocrystalline scintillators with a commercial CCD.[118] This scintillator achieved a detection limit of 40.1 nGy_{air} s^{-1}, and can stably work for 108 h at continuous X-ray irradiation (dose rate of 5.5 μGy_{air} s^{-1}). Figure 14k displays schematically the imaging systems, where the as-prepared scintillator was placed between the detected object and the commer-

cial CCD. Because of the different X-ray stopping abilities on objects, scintillators received X-rays with different intensities and then converted them to visible lights that were collected by commercial CCD. The spatial resolution of scintillators was evaluated by MTF extracted from the slanted edge in X-ray images, as summarized in Figure 14l. Figure 14m displays the photographs of scintillators with different thicknesses and corresponding X-ray imaging results. The highest resolution of 17.3 lp mm^{-1} (MTF is 0.2) was realized with a scintillator thickness of 0.01 mm, which is higher than the commercial CsI:Tl flat-panel X-ray detectors (10 lp mm^{-1}).[119]

5. Conclusion and Outlook

In this review, the recent developments of wavelength-selective perovskite PDs and their applications in image sensing are systematically introduced. The main performances of wavelength-selective perovskite PDs have been rapidly improved in recent years: 1) the FWHM of spectral response for narrowband PDs narrows to about 12 nm from 100 nm at the beginning of the study;[21,56] 2) both negative and positive photoresponses related to light wavelengths are implemented in a single dual-band PD;[87] 3) multispectral-recognizable PDs enable simultaneous detection of light intensity and spectra, which attributes comparable to commercial spectrometers;[93] 4) ultrahigh sensitivity of perovskite X-ray PD is obtained, which is three orders of magnitude higher than the reported α-Se X-ray detectors.[102] In terms of applications, the state-of-the-art multispectral-recognizable PDs and X-ray detectors exhibit the capability of full-color imaging and high-resolution X-ray imaging, respectively.[40,115] All of these are attributed to the controllable synthesis of high-quality perovskite materials and the proposal of new mechanisms.

Some challenges remain for wavelength-selective perovskite PDs to meet practical applications. 1) Although a series of perovskite narrowband PDs have been assembled, the integration of narrowband PDs with different recognition wavelength bands, such as red, green, and blue on a single monolithic substrate, is still a challenge. Perovskite materials are not compatible with micro-nanofabrication technologies involving polar liquids, thus novel device processing methods for integrating narrowband perovskite PDs are desired. The realization of this goal can extend their application to panchromatic imaging. 2) Most of the wavelength-selective PDs reported so far are device demonstrations with few pixel numbers and low resolution. Employing the device structure of cross-type is the efficient path to exploit devices with large-scale and high-resolution. The assembly of such a device could significantly optimize imaging quality. For the miniatured spectral detectors reported by Xu et al., their spectral resolution could be further improved by increasing the pixel numbers. 3) The toxicity of Pb in lead halide perovskites seriously limits their applications. Especially, the X-ray detectors have vital applications in medical diagnosis, it is urgent to reduce the possible harm caused by heavy metal Pb to the environment and organisms. Lead-free perovskite detectors can be used as alternatives, but their performances need further improvement. In addition, it is possible pathway to solve this problem by developing effective encapsulation technology of preventing Pb leaks.

Acknowledgements

The authors thank the support of the Shenzhen Science and Technology Program (Grant No. KQTD20170810105439418), National Natural Science Foundation of China (Nos. 52125205, U20A20166, 52192614, U22A2077, and 52002246), National Key R&D Program of China (Nos. 2021YFB3200302 and 2021YFB3200304), Natural Science Foundation of Beijing Municipality (Nos. Z180011 and 2222088), Project funded by China Postdoctoral Science Foundation (No. 2022M712166), the Shenzhen Fundamental Research Project (No. JCYJ20190808170601664), the Science and Technology Innovation Project of Shenzhen Excellent Talents (No. RCBS20200714114919006), and the Fundamental Research Funds for the Central Universities.

Conflict of Interest

The authors declare no conflict of interest.

Keywords

image sensing, metal halide perovskites, photodetectors, wavelength recognition, X-ray imaging

Received: November 15, 2022
Revised: January 18, 2023
Published online: February 21, 2023

[1] R. D. Jansen-van Vuuren, A. Armin, A. K. Pandey, P. L. Burn, P. Meredith, *Adv. Mater.* **2016**, *28*, 4766.
[2] C. L. Li, Y. Ma, Y. F. Xiao, L. Shen, L. M. Ding, *InfoMat* **2020**, *2*, 1247.
[3] I. Ryu, J. Y. Ryu, G. Choe, H. Kwon, H. Park, Y. S. Cho, R. S. Du, S. Yim, *Adv. Funct. Mater.* **2021**, *31*, 2102334.
[4] F. Cao, T. T. Yan, Z. Q. Li, L. M. Wu, X. S. Fang, *Adv. Opt. Mater.* **2022**, *10*, 2200786.
[5] L. D. Li, S. Ye, J. L. Qu, F. F. Zhou, J. Song, G. Z. Shen, *Small* **2021**, *17*, 2005606.
[6] Z. L. Zhang, Y. Tian, J. X. Li, Y. P. Xu, *Remote Sens.* **2022**, *14*, 1513.
[7] J. Jang, S. Ji, G. K. Grandhi, H. B. Cho, W. B. Im, J. U. Park, *Adv. Mater.* **2021**, *33*, 2008539.
[8] X. Han, Z. S. Xu, W. Q. Wu, X. H. Liu, P. G. Yan, C. F. Pan, *Small Struct.* **2020**, *1*, 2000029.
[9] Y. Y. Peng, N. Yang, Q. Xu, Y. Dai, Z. Q. Wang, *Sensors* **2021**, *21*, 5392.
[10] K. M. M. Rahman, S. K. Mohammed, S. S. Vedaei, M. R. Mohebbian, F. S. Chafjiri, K. A. Wahid, *Signal Image Video Process* **2021**, *15*, 1767.
[11] Y. Monno, S. Kikuchi, M. Tanaka, M. Okutomi, *IEEE Trans. On Image Process.* **2015**, *24*, 3048.
[12] J. C. Zhuang, X. Xu, H. F. Feng, Z. Li, X. L. Wang, Y. Du, *Sci. Bull.* **2015**, *60*, 1551.
[13] H. Huang, S. Abbaszadeh, *IEEE Sens. J.* **2020**, *20*, 1694.
[14] F. G. Zhou, Z. Z. Li, W. Lan, Q. Wang, L. M. Ding, Z. W. Jin, *Small Methods* **2020**, *4*, 2000506.
[15] K. Wang, H. Zhang, Z. Gu, *Sci. Bull.* **2019**, *64*, 1205.
[16] Q. Xu, J. Huang, J. Liu, J. Wang, S. Zhou, X. Wang, J. Nie, Y. Guo, X. P. Ouyang, *Nanotechnology* **2021**, *32*, 205201.
[17] W. Q. Wu, X. D. Wang, X. Han, Z. Yang, G. Y. Gao, Y. F. Zhang, J. F. Hu, Y. W. Tan, A. L. Pan, C. F. Pan, *Adv. Mater.* **2019**, *31*, 1805913.
[18] X. P. Feng, Y. H. He, W. Qu, J. M. Song, W. T. Pan, M. R. Tan, B. Yang, H. T. Wei, *Nat. Commun.* **2022**, *13*, 6106.
[19] Z. Yang, M. M. Jiang, L. J. Guo, G. F. Hu, Y. S. Gu, J. G. Xi, Z. H. Huo, F. T. Li, S. F. Wang, C. F. Pan, *Nano Energy* **2021**, *85*, 105951.
[20] D. F. Peng, X. H. Liu, C. F. Pan, *Sci. Bull.* **2021**, *66*, 6.

[21] Q. Q. Lin, A. Armin, P. L. Burn, P. Meredith, *Nat. Photonics* **2015**, *9*, 687.
[22] A. Jana, S. Cho, S. A. Patil, A. Meena, Y. Jo, V. G. Sree, Y. Park, H. Kim, H. Im, R. A. Taylor, *Mater. Today* **2022**, *55*, 110.
[23] S. Yakunin, M. Sytnyk, D. Kriegner, S. Shrestha, M. Richter, G. J. Matt, H. Azimi, C. J. Brabec, J. Stangl, M. V. Kovalenko, W. Heiss, *Nat. Photonics* **2015**, *9*, 444.
[24] Y. Li, D. Kuang, J. Guo, B. Liu, Y. Zhang, S. Xu, X. W. Liu, X. Y. Li, Z. N. Yu, *J. Alloys Compd.* **2022**, *904*, 163990.
[25] L. Q. Guo, H. X. Sun, M. Wang, M. Wang, L. L. Min, F. R. Cao, W. Tian, L. Li, *Adv. Mater.* **2022**, *34*, 2200221.
[26] X. B. Xu, Y. H. Dong, Y. Z. Zhang, Z. Y. Han, J. X. Liu, D. J. Yu, Y. Wei, Y. S. Zou, B. Huang, J. Chen, H. B. Zeng, *Nano Res.* **2022**, *15*, 5476.
[27] X. Han, W. Q. Wu, H. Chen, D. F. Peng, L. Qiu, P. G. Yan, C. F. Pan, *Adv. Funct. Mater.* **2021**, *31*, 2005230.
[28] Y. Zhang, Y. Ma, Y. Wang, X. Zhang, C. Zuo, L. Shen, L. Ding, *Adv. Mater.* **2021**, *33*, 2006691.
[29] Z. Lan, Y. S. Lau, Y. Wang, Z. Xiao, L. Ding, D. Luo, F. Zhu, *Adv. Opt. Mater.* **2020**, *8*, 2001388.
[30] H. D. Wu, Y. S. Ge, G. D. Niu, J. Tang, *Matter* **2021**, *4*, 144.
[31] X. Xu, W. Qian, S. Xiao, J. Wang, S. Zheng, S. Yang, *EcoMat* **2020**, *2*, e12064.
[32] Y. Zhou, J. Chen, O. M. Bakr, O. F. Mohammed, *ACS Energy Lett.* **2021**, *6*, 739.
[33] H. M. Chen, J. R. Chen, M. H. Li, M. H. You, Q. S. Chen, M. J. Lin, H. H. Yang, *Chem* **2022**, *65*, 2338.
[34] M. D. Birowosuto, D. Cortecchia, W. Drozdowski, K. Brylew, W. Lachmanski, A. Bruno, C. Soci, *Sci. Rep.* **2016**, *6*, 37254.
[35] S. S. Tan, C. Y. Liu, Y. L. Jiang, D. Y. Lin, K. Y. J. Hsu, *Appl. Phys. Lett.* **2009**, *94*, 171103.
[36] P. Lecoq, *Nucl. Instrum. Methods Phys. Res. A* **2016**, *809*, 130.
[37] K. Shibuya, M. Koshimizu, Y. Takeoka, K. Asai, *Nucl. Instrum. Methods Phys. Res., Sect. B* **2002**, *194*, 207.
[38] M. I. Saidaminov, M. A. Haque, M. Savoie, A. L. Abdelhady, N. Cho, I. Dursun, U. Buttner, E. Alarousu, T. Wu, O. M. Bakr, *Adv. Mater.* **2016**, *28*, 8144.
[39] J. Wang, J. Z. Li, S. G. Lan, C. Fang, H. Z. Shen, Q. H. Xiong, D. H. Li, *ACS Nano* **2019**, *13*, 5473.
[40] X. B. Xu, Z. Y. Han, Y. S. Zou, J. Y. Li, Y. Gu, D. W. Hu, Y. He, J. X. Liu, D. J. Yu, F. Cao, H. B. Zeng, *Adv. Mater.* **2022**, *34*, 2108408.
[41] H. T. Wei, Y. J. Fang, P. Mulligan, W. Chuirazzi, H. H. Fang, C. C. Wang, B. R. Ecker, Y. L. Gao, M. A. Loi, L. Cao, J. S. Huang, *Nat. Photonics* **2016**, *10*, 333.
[42] B. M. Xie, R. H. Xie, K. Zhang, Q. W. Yin, Z. C. Hu, G. Yu, F. Huang, Y. Cao, *Nat. Commun.* **2020**, *11*, 2871.
[43] R. J. van Vuuren, K. D. Johnstone, S. Ratnasingam, H. Barcena, P. C. Deakin, A. K. Pandey, P. L. Burn, S. Collins, I. D. W. Samuel, *Appl. Phys. Lett.* **2010**, *96*, 253303.
[44] S. J. Lim, D. S. Leem, K. B. Park, K. S. Kim, S. Sul, K. Na, G. H. Lee, C. J. Heo, K. H. Lee, X. Bulliard, R. I. Satoh, T. Yagi, T. Ro, D. Im, J. Jung, M. Lee, T. Y. Lee, M. G. Han, Y. WanJin, S. Lee, *Sci. Rep.* **2015**, *5*, 7708.
[45] L. Wang, H. H. Luo, H. H. Zuo, J. Q. Tao, Y. Q. Yu, X. P. Yang, M. L. Wang, J. G. Hu, C. Xie, D. Wu, L. B. Luo, *IEEE Trans. Electron Devices* **2020**, *67*, 3211.
[46] W. H. Li, D. Li, G. F. Dong, L. Duan, J. L. Sun, D. Q. Zhang, L. D. Wang, *Laser Photonics Rev.* **2016**, *10*, 473.
[47] J. Vanderspikken, W. Maes, K. Vandewal, *Adv. Funct. Mater.* **2021**, *31*, 2104060.
[48] M. Knupfer, *Appl. Phys.* **2003**, *77*, 623.
[49] V. Pecunia, *J. Phys. Mater.* **2019**, *2*, 042001.
[50] K. Kuribara, H. Wang, N. Uchiyama, K. Fukuda, T. Yokota, U. Zschieschang, C. Jaye, D. Fischer, H. Klauk, T. Yamamoto, K. Takimiya, M. Ikeda, H. Kuwabara, T. Sekitani, Y. L. Loo, T. Someya, *Nat. Commun.* **2012**, *3*, 723.
[51] P. C. Y. Chow, T. Someya, *Adv. Mater.* **2020**, *32*, 1902045.
[52] L. Li, L. Jin, Y. X. Zhou, J. Z. Li, J. Q. Ma, S. Wang, W. C. Li, D. H. Li, *Adv. Opt. Mater.* **2019**, *7*, 1900988.
[53] Y. Wu, X. M. Li, Y. Wei, Y. Gu, H. B. Zeng, *Nanoscale* **2018**, *10*, 359.
[54] Y. D. Tu, Y. Xu, J. Z. Li, Q. Y. Hao, X. S. Liu, D. Y. Qi, C. X. Bao, T. C. He, F. Gao, W. J. Zhang, *Small* **2020**, *16*, 2005626.
[55] W. Q. Wu, X. Han, J. Li, X. D. Wang, Y. F. Zhang, Z. H. Huo, Q. S. Chen, X. D. Sun, Z. S. Xu, Y. W. Tan, C. F. Pan, A. L. Pan, *Adv. Mater.* **2021**, *33*, 2006006.
[56] J. Xue, Z. F. Zhu, X. B. Xu, Y. Gu, S. L. Wang, L. M. Xu, Y. S. Zou, J. Z. Song, H. B. Zeng, Q. Chen, *Nano Lett.* **2018**, *18*, 7628.
[57] W. L. Tsai, C. Y. Chen, Y. T. Wen, L. Yang, Y. L. Cheng, H. W. Lin, *Adv. Mater.* **2019**, *31*, 1900231.
[58] L. L. Li, Y. H. Deng, C. X. Bao, Y. J. Fang, H. T. Wei, S. Tang, F. J. Zhang, J. S. Huang, *Adv. Opt. Mater.* **2017**, *5*, 1700672.
[59] P. Zhang, Y. Q. Hua, X. Li, L. Z. Zhang, L. Liu, R. Z. Li, G. D. Zhang, X. T. Tao, *J. Mater. Chem. C* **2021**, *9*, 2840.
[60] H. S. Rao, W. G. Li, B. X. Chen, D. B. Kuang, C. Y. Su, *Adv. Mater.* **2017**, *29*, 1602639.
[61] P. Liu, Y. Liu, S. W. Zhang, J. Z. Li, C. Y. Wang, C. Zhao, P. B. Nie, Y. H. Dong, X. Zhang, S. X. Zhao, G. D. Wei, *Adv. Opt. Mater.* **2020**, *8*, 2001072.
[62] X. Wang, Y. Z. Pan, Y. B. Xu, J. D. Zhao, Y. W. Li, Q. Li, J. Chen, Z. W. Zhao, X. B. Zhang, E. E. Elemike, D. C. Onwudiwe, B. S. Bae, W. Lei, *Adv. Electron. Mater.* **2022**, *8*, 2200178.
[63] Y. J. Fang, Q. F. Dong, Y. C. Shao, Y. B. Yuan, J. S. Huang, *Nat. Photonics* **2015**, *9*, 679.
[64] D. Q. Zhang, Y. D. Zhu, Q. P. Zhang, B. T. Ren, B. Y. Cao, Q. Z. Li, S. Poddar, Y. Zhou, X. Qiu, Z. B. He, Z. Y. Fan, *Nano Lett.* **2022**, *22*, 3062.
[65] Y. N. Chen, Y. Sun, J. J. Peng, J. H. Tang, K. B. Zheng, Z. Q. Liang, *Adv. Mater.* **2018**, *30*, 1703487.
[66] H. Z. Wang, L. Li, J. Q. Ma, J. Z. Li, D. H. Li, *J. Mater. Chem. C* **2021**, *9*, 11085.
[67] J. Z. Li, J. Wang, J. Q. Ma, H. Z. Shen, L. Li, X. F. Duan, D. H. Li, *Nat. Commun.* **2019**, *10*, 806.
[68] Y. Zhao, C. L. Li, L. Shen, *Chin. Phys. B* **2018**, *27*, 127806.
[69] J. H. Heo, S. H. Im, *Adv. Mater.* **2016**, *28*, 5121.
[70] J. Wang, S. Xiao, W. Qian, K. Zhang, J. Yu, X. W. Xu, G. P. Wang, S. Z. Zheng, S. H. Yang, *Adv. Mater.* **2021**, *33*, 2005557.
[71] Y. C. Hou, C. C. Wu, X. Huang, D. Yang, T. Ye, J. Yoon, R. Sriramdas, K. Wang, S. Priya, *Adv. Funct. Mater.* **2021**, *31*, 2007016.
[72] X. D. Liu, Y. W. Lin, Y. J. Liao, J. Z. Wu, Y. H. Zheng, *J. Mater. Chem. C* **2018**, *6*, 3499.
[73] S. Qiao, Y. Liu, J. H. Liu, G. S. Fu, S. F. Wang, *ACS Appl. Mater. Interfaces* **2021**, *13*, 34625.
[74] F. Cao, J. D. Chen, D. J. Yu, S. Wang, X. B. Xu, J. X. Liu, Z. Y. Han, B. Huang, Y. Cu, K. L. Choy, H. B. Zeng, *Adv. Mater.* **2020**, *32*, 1905362.
[75] G. R. Yettapu, D. Talukdar, S. Sarkar, A. Swarnkar, A. Nag, P. Ghosh, P. Mandal, *Nano Lett.* **2016**, *16*, 4838.
[76] C. C. Stoumpos, C. D. Malliakas, J. A. Peters, Z. F. Liu, M. Sebastian, J. Im, T. C. Chasapis, A. C. Wibowo, D. Y. Chung, A. J. Freeman, B. W. Wessels, M. G. Kanatzidis, *Cryst. Growth Des.* **2013**, *13*, 2722.
[77] A. Sobhani, M. W. Knight, Y. M. Wang, B. Zheng, N. S. King, L. V. Brown, Z. Y. Fang, P. Nordlander, N. J. Halas, *Nat. Commun.* **2013**, *4*, 1643.
[78] D. Wu, R. F. Li, Y. M. Liu, Z. Y. Yu, L. Yu, L. Chen, C. Liu, R. Ma, H. Ye, *Nanoscale Res. Lett.* **2017**, *12*, 427.
[79] C. C. Wu, B. W. Du, W. Luo, Y. Liu, T. Y. Li, D. Wang, X. Guo, H. Ting, Z. Fang, S. F. Wang, Z. J. Chen, Y. X. Chen, L. X. Xiao, *Adv. Opt. Mater.* **2018**, *6*, 1800811.

[80] J. Wang, X. W. Xu, S. Xiao, Y. Li, W. Qian, J. Yu, K. Zhang, S. H. Yang, *Adv. Opt. Mater.* **2021**, *9*, 2100517.
[81] X. Z. Xu, W. Deng, X. J. Zhang, L. M. Huang, W. Wang, R. F. Jia, D. Wu, X. H. Zhang, J. S. Jie, S. T. Lee, *ACS Nano* **2019**, *13*, 5910.
[82] Y. Gao, C. Zhao, K. Pu, M. He, W. Cai, M.-C. Tang, F. Kang, H.-L. Yip, G. Wei, *Sci. Bull.* **2022**, *67*, 1982.
[83] B. Huang, J. X. Liu, Z. Y. Han, Y. Gu, D. J. Yu, X. B. Xu, Y. S. Zou, *ACS Appl. Mater. Interfaces* **2020**, *12*, 48765.
[84] K. Wang, H. F. Hu, S. Lu, M. H. Jin, Y. J. Wang, T. He, *Appl. Phys. Lett.* **2020**, *116*, 203107.
[85] K. Swaminathan, T. J. Grassman, L. M. Yang, Q. Gu, M. J. Mills, S. A. Ringel, *J. Appl. Phys.* **2011**, *110*, 063109.
[86] J. L. Miao, F. J. Zhang, *Laser Photonics Rev.* **2019**, *13*, 1800204.
[87] L. Li, H. Y. Chen, Z. M. Fang, X. Y. Meng, C. T. Zuo, M. L. Lv, Y. Z. Tian, Y. Fang, Z. Xiao, C. X. Shan, Z. G. Xiao, Z. W. Jin, G. Z. Shen, L. Shen, L. M. Ding, *Adv. Mater.* **2020**, *32*, 1907257.
[88] X. Zhou, C. Wang, J. Luo, L. Zhang, F. Zhao, Q. Ke, *Chem. Eng. J.* **2022**, *450*, 136364.
[89] F. Cao, Z. Li, X. Liu, Z. Shi, X. Fang, *Adv. Funct. Mater.* **2022**, *32*, 2206151.
[90] Z. S. Lv, Z. K. Liao, H. Jiang, *IEEE Electron Dev. Lett.* **2021**, *42*, 1362.
[91] A. Taruttis, V. Ntziachristos, *Nat. Photonics* **2015**, *9*, 219.
[92] X. Y. Yu, H. N. Tsao, Z. L. Zhang, P. Gao, *Adv. Opt. Mater.* **2020**, *8*, 202001095.
[93] M. N. Zhang, X. H. Wu, A. Riaud, X. L. Wang, F. X. Xie, W. J. Liu, Y. F. Mei, D. W. Zhang, S. J. Ding, *Light: Sci. Appl.* **2020**, *9*, 162.
[94] V. R. F. Schroder, F. Hermerschmidt, S. Helper, C. Rehermann, G. Ligorio, H. Nasstrom, E. L. Unger, E. J. W. List-Kratochvil, *Adv. Eng. Mater.* **2022**, *24*, 2101111.
[95] Y. T. Chen, C. Y. Zhao, T. T. Zhang, X. H. Wu, W. J. Zhang, S. J. Ding, *Small* **2021**, *17*, 2007543.
[96] Q. L. Wang, G. N. Zhang, H. Y. Zhang, Y. Q. Duan, Z. P. Yin, H. A. Huang, *Adv. Funct. Mater.* **2021**, *31*, 2100857.
[97] H. X. Sun, W. Tian, X. F. Wang, K. M. Deng, J. Xiong, L. Li, *Adv. Mater.* **2020**, *32*, 1908108.
[98] A. Datta, Z. Zhong, S. Motakef, *Sci. Rep.* **2020**, *10*, 20097.
[99] X. M. Li, C. F. Meng, B. Huang, D. D. Yang, X. B. Xu, H. B. Zeng, *Adv. Opt. Mater.* **2020**, *8*, 2000273.
[100] S. Shrestha, R. Fischer, G. J. Matt, P. Feldner, T. Michel, A. Osvet, I. Levchuk, B. Merle, S. Golkar, H. W. Chen, S. F. Tedde, O. Schmidt, R. Hock, M. Ruhrig, M. Goken, W. Heiss, G. Anton, C. J. Brabec, *Nat. Photonics* **2017**, *11*, 436.
[101] L. L. Liu, W. J. Li, X. P. Feng, C. J. Guo, H. M. Zhang, H. T. Wei, B. Yang, *Adv. Sci.* **2022**, *9*, 202103735.
[102] W. Wei, Y. Zhang, Q. Xu, H. T. Wei, Y. J. Fang, Q. Wang, Y. H. Deng, T. Li, A. Gruverman, L. Cao, J. S. Huang, *Nat. Photonics* **2017**, *11*, 315.
[103] J. J. Zhao, L. Zhao, Y. H. Deng, X. Xiao, Z. Y. Ni, S. Xu, J. S. Huang, *Nat. Photonics* **2020**, *14*, 612.
[104] Y. C. Kim, K. H. Kim, D. Y. Son, D. N. Jeong, J. Y. Seo, Y. S. Choi, I. T. Han, S. Y. Lee, N. G. Park, *Nature* **2017**, *550*, 87.
[105] E. Samei, M. J. Flynn, D. A. Reimann, *Med. Phys.* **1998**, *25*, 102.
[106] M. L. Xia, Z. H. Song, H. D. Wu, X. Y. Du, X. He, J. C. Pang, H. D. Luo, L. B. Jin, G. F. Li, G. D. Niu, J. Tang, *Adv. Funct. Mater.* **2022**, *32*, 2110729.
[107] P. Zhang, Y. Q. Hua, Y. D. Xu, Q. H. Sun, X. Li, F. C. Cui, L. Liu, Y. X. Bi, G. D. Zhang, X. T. Tao, *Adv. Mater.* **2022**, *34*, 2106562.
[108] C. Szeles, *Phys. Status Solidi B* **2004**, *241*, 783.
[109] J. A. Rowlands, *Nature* **2017**, *550*, 47.
[110] Z. J. Zhang, H. Dierks, N. Lamers, C. Sun, K. Novakova, C. Hetherington, I. G. Scheblykin, J. Wallentin, *ACS Appl. Nano Mater.* **2022**, *5*, 881.
[111] W. Q. Chen, M. Zhou, Y. Liu, X. Yu, C. J. Pi, Z. Yang, H. Zhang, Z. C. Liu, T. Wang, J. B. Qiu, S. F. Yu, Y. Yang, X. H. Xu, *Adv. Funct. Mater.* **2022**, *32*, 2107424.
[112] Y. Y. Wang, H. R. Lou, C. Y. Yue, X. W. Lei, *CrystEngComm* **2022**, *24*, 2201.
[113] Z. Yang, T. Albrow-Owen, H. Cui, J. Alexander-Webber, F. Gu, X. Wang, T.-C. Wu, M. Zhuge, C. Williams, P. Wang, *Science* **2019**, *365*, 1017.
[114] Q. Wang, Q. Zhou, M. Nikl, J. W. Xiao, R. Kucerkova, A. Beitlerova, V. Babin, P. Prusa, V. Linhart, J. K. Wang, X. M. Wen, G. D. Niu, J. Tang, G. H. Ren, Y. T. Wu, *Adv. Opt. Mater.* **2022**, *10*, 2200304.
[115] S. Deumel, A. van Breemen, G. Gelinck, B. Peeters, J. Maas, R. Verbeek, S. Shanmugam, H. Akkerman, E. Meulenkamp, J. E. Huerdler, M. Acharya, M. Garcia-Batlle, O. Almora, A. Guerrero, G. Garcia-Belmonte, W. Heiss, O. Schmidt, S. F. Tedde, *Nat. Electron.* **2021**, *4*, 681.
[116] Y. C. Liu, Y. X. Zhang, X. J. Zhu, J. S. Feng, I. Spanopoulos, W. J. Ke, Y. H. He, X. D. Ren, Z. Yang, F. W. Xiao, K. Zhao, M. Kanatzidis, S. Z. Liu, *Adv. Mater.* **2021**, *33*, 2006010.
[117] M. X. Hu, S. S. Jia, Y. C. Liu, J. Cui, Y. X. Zhang, H. Su, S. Q. Cao, L. H. Mo, D. P. Chu, G. T. Zhao, K. Zhao, Z. Yang, S. F. Liu, *ACS Appl. Mater. Interfaces* **2020**, *12*, 16592.
[118] B. Q. Wang, J. L. Peng, X. Yang, W. S. Cai, H. B. Xiao, S. Y. Zhao, Q. Q. Lin, Z. G. Zang, *Laser Photonics Rev.* **2022**, *16*, 2100736.
[119] C. C. Stoumpos, C. D. Malliakas, J. A. Peters, Z. Liu, M. Sebastian, J. Im, T. C. Chasapis, A. C. Wibowo, D. Y. Chung, A. J. Freeman, B. W. Wessels, M. G. Kanatzidis, *Cryst. Growth Des.* **2013**, *13*, 2722.

Wenqiang Wu received his Ph.D. degree from the College of Materials Science and Engineering, Hunan University in 2021. Currently, he carries out postdoctoral research work at the Institute of Microscale Optoelectronics, Shenzhen University. His research focuses on the controllable synthesis of perovskite materials and their applications in high-performance optoelectronic devices.

Caofeng Pan received his B.S. degree (2005) and his Ph.D. (2010) in materials science and engineering from Tsinghua University, China. He then joined the Georgia Institute of Technology as a postdoctoral fellow. He is currently a professor and a group leader at Beijing Institute of Nanoenergy and Nanosystems, Chinese Academy of Sciences since 2013. His main research interests focus on the fields of piezotronics/piezo-phototronics for fabricating new electronic and optoelectronic devices, nanopower source (such as nanofuel cell, nano biofuel cell, and nanogenerator), hybrid nanogenerators, and self-powered nanosystems.http://www.piezotronics.cn